



**A Coherent, Polarimetric SAR Simulation of Forests
for
PolSARPro**

Design Document and Algorithm Specification (u1.0)



Dr Mark L. Williams
mark.williams@physics.org

October 2006

1 Contents

1	Contents	2
2	Executive Summary	4
3	Introduction	6
3.1	General	6
3.2	PolSARproSim Concept	7
3.3	Capability Statement	8
3.4	Notable Features of PolSARproSim	8
3.5	Flow Chart for PolSARproSim Operation	10
4	General Considerations	11
4.1	Terrain and Imaging Geometry	11
4.2	Input Parameters	12
4.3	SAR Imaging Geometry	12
4.4	SAR Image dimensions	13
5	DEM Generation	15
5.1	Introduction	15
5.2	Theory	15
5.3	DEM Generation Algorithm	16
5.4	DEM Generation Summary	18
5.5	Choice of Large-Scale Surface Roughness	18
6	Tree Location Map Generation	20
6.1	Introduction	20
6.2	Algorithm Details	20
6.3	Tree Location Map Summary	22
6.4	Special Note on the HEDGE Option	22
7	Tree Species and Architecture	23
7.1	Introduction	23
7.2	Trees	23
7.3	Branches	24
7.4	Crowns	25
7.5	Realization of Trees	26
7.6	Generating Stems and Branches	26
8	Interferometric SAR Image Calculation	28
8.1	Introduction	28
8.2	Representation of the SAR Image	29
8.3	Modelling Attenuation	31
8.4	Direct-Ground (DG) SAR Image	32
8.5	Choice of Small-Scale Parameters	33
8.6	The DG Imaging Algorithm	34
8.7	XBragg on a Tilted Surface	39
8.8	DG Algorithm Summary	40
8.9	Direct-Vegetation (DV) and Direct-Forest (DF) SAR Images	40
8.10	Deterministic Model	40
8.11	Hybrid Stochastic Model	40
8.12	Surface-Vegetation (SV) and Surface-Forest (SF) SAR Images	41
8.13	Summary of Input Parameters	42
9	File Formats and Calling Convention	43
9.1	Introduction	43
9.2	Input Text File	43

9.3	PolSARproSim Calling Convention.....	45
9.4	Graphic File Format.....	46
9.5	Image File Format.....	47
10	References.....	49
11	Appendix A: Finding Ray Intersections	52
11.1	General.....	52
11.2	Intersection with a Plane.....	52
11.3	Intersection with a Cylinder.....	52
11.4	Intersection with a Cone	53
11.5	Intersection with a Spheroid	54

2 Executive Summary

- 2.1.1 This document describes the software package **PolSARproSim**, designed to calculate simulated synthetic aperture radar (SAR) imagery of model forest stands. It is delivered to the University of Rennes as part of the documentation for the contract "PolInSAR Coherent Scattering and Imaging Code Development", 2006. This document serves as a reference, and as a general guide to the construction and operation of **PolSARproSim**, and a description of the algorithms coded. This document is not definitive but serves as a broad definition of overall capability, and contains many details of the implementation.
- 2.1.2 The document is divided into a number of sections. The introduction contains a statement of capability; a high-level description of **PolSARproSim**, describing the concept, its operation and the user-interface in general terms.
- 2.1.3 Following the introduction is a detailed, task-oriented description of the implementation of **PolSARproSim**. This is naturally divided into a number of stages: receipt of parameters describing the forest and SAR imaging process, construction of the forest, and calculation and output of the SAR images. Forest construction and SAR imaging processes are described first and a list of required parameters is generated during the discussion. This list is summarized at the end of the section on implementation.
- 2.1.4 **PolSARproSim** is designed to be an educational tool: providing simulated test data of sufficient fidelity to be used within the tutorial package of **PolSARPro v2.0**. In designing **PolSARproSim** and drawing up this document it has been anticipated that the user is sophisticated, yet not an expert in either forestry or PolInSAR techniques. The user has therefore been given limited but sufficient influence, via a simple interface, over those parameters controlling the nature of the forest and the SAR imaging sensor.
- 2.1.5 The users' interface is implemented within **PolSARPro v2.0**, and numerical parameter values collected within **PolSARPro v2.0** are passed to **PolSARproSim** via a text file. Following input of the parameters **PolSARproSim** performs the requested simulations, generating an interferometric pair of fully polarimetric SAR images, and writing them to file, in binary format, for input back into **PolSARPro v2.0** for post-processing using PolInSAR techniques.
- 2.1.6 To make **PolSARproSim** available on any machine capable of running **PolSARPro v2.0** the code has been written in ANSI standard C, and source code will be delivered that may be compiled as required for delivery on different platforms.
- 2.1.7 All the code is new and has been written specifically for the contract "PolInSAR Coherent Scattering and Imaging Code Development", 2006. All the algorithms encoded are either described fully in the open literature, or are versions of open literature techniques modified according to new ideas generated under the contract.

- 2.1.8 Since the full variety of platforms may not be anticipated **PolSARproSim** is designed to have the smallest possible memory footprint, whilst maintaining efficiency of execution.



Dr Mark L. Williams
(mark.williams@physics.org)

3 Introduction

3.1 General

- 3.1.1 The computer simulation of SAR images of forest is not a new technique and capabilities already exist in the USA, France, the Netherlands and Finland, which use accurate tree models. Details of the theory and techniques required to simulate forest SAR imagery have been published widely in the open literature, and the interested reader is referred to the reference section for further reading (particularly Cloude, Corr and Williams, 2004, and Varenkamp, 2005).
- 3.1.2 The availability of substantial computer power on a desktop or even notebook machine, coupled with efficiency of coding and algorithmic simplicity, has helped to bring this capability to the scientific community.
- 3.1.3 The techniques described here follow a physics-based approach to the simulation of SAR imagery. The starting point is a detailed (but limited) physical description of the scene, including in addition to geometry such quantities as surface roughness and the frequency-dependent dielectric behaviour of materials. Theoretical attenuation and scattering models for each element of the artificial 3D scene are combined with a model for coherent SAR imaging to construct images as coherent sums of focused scattering events.
- 3.1.4 Images simulated in this way display properties consistent with those observed in real SAR imagery. In particular the simulated backscattering coefficients, speckle distributions, shadowing, polarimetric and interferometric coherence properties may all be simulated with a high level of realism.
- 3.1.5 One should always remember that the simulated data is not real and contains many approximations. For example each scatterer is assumed to scatter the mean field, not all scattering processes are included, the attenuation suffered by the coherent field is modelled only approximately, and the images contain no incoherent noise or system error artefacts. In this sense the imagery is “idealised”, yet its fidelity makes it ideal for teaching purposes.

3.2 *PolSARproSim Concept*

- 3.2.1 **PolSARproSim** is designed to be an educational tool: providing simulated test data of sufficient fidelity to be used within the tutorial package of **PolSARPro v2.0**. The purpose of the simulation is to provide simulated SAR images to illustrate the concepts of the PolInSAR lecture course.
- 3.2.2 The simulation is designed to overcome the limited availability of suitable data, and thereby remove an obstacle to learning. Whilst it would be possible to incorporate many examples of data with **PolSARPro v2.0** software, it is not feasible to anticipate all the situations of interest to potential users: hence the simulation capability.
- 3.2.3 The user is provided with a simple interface that permits the ready description of a realistic forest model, and a flexible description of SAR imaging parameters. Having designed the forest and set the imaging scenario the simulation is called from within **PolSARPro v2.0**, and in a short space of time (depending upon computer platform) the user has available simulated polarimetric, interferometric SAR data for the scene and sensor of their choice.
- 3.2.4 The graphical user interface (GUI) used to assign parameter values is implemented within **PolSARPro v2.0**. A list of parameter values chosen by the user is communicated to the SAR simulation software via a text file. **PolSARproSim** is then called from within **PolSARPro v2.0** (with the output location under user control).
- 3.2.5 In addition to the final polarimetric, interferometric SAR imagery, **PolSARproSim** generates additional files. For example a digital elevation map (DEM) file is generated, as is a list of stem locations and heights with crown dimensions. When notified that the images are ready, the user may proceed to analyse the imagery using the algorithms from within **PolSARPro v2.0**.
- 3.2.6 The following is a short, high-level statement of capability for **PolSARproSim**:

3.3 *Capability Statement*

- 3.3.1 **PolSARproSim** is called from within **PolSARPro v2.0** to perform SAR imaging calculations of a model forest.
- 3.3.2 Parameters controlling the operation of **PolSARproSim** are passed via a text file from **PolSARPro v2.0** having been gathered from within **PolSARPro v2.0** via a graphical user interface.
- 3.3.3 **PolSARproSim** uses the parameter file values to construct a scene to be imaged, including a digital elevation map, and an array of trees, with specified surface and forest properties, such as ground roughness and the mean height of the forest stand. The description of the forest scene is reported.
- 3.3.4 **PolSARproSim** then proceeds to use the parameter file values to calculate an interferometric pair of SAR images of the forest using those SAR sensor values and interferometric baseline requested by the user. These images are output in a binary format suitable for analysis within **PolSARPro v2.0**, along with a record of ancillary information describing the imaging scenario, such as range to scene centre, centre frequency and baseline etc., into a text file.

3.4 *Notable Features of PolSARproSim*

- 3.4.1 Key features in the design of **PolSARproSim** are intended ease of use, minimum memory requirements, maximum speed of execution, and fidelity of simulated imagery sufficient for the educational requirement.
- 3.4.2 **PolSARproSim** is written in ANSI C to help maintain portability across platforms.
- 3.4.3 Memory requirements are minimized during execution by storing only a single realization of tree architecture at any time, and by treating small plant scattering elements using stochastic techniques that preserve interferometric coherence.
- 3.4.4 Execution speed is optimised by using simplified forms for scattering by plant elements determined by size, and by modelling tree crowns as having uniform mean effective permittivity, thereby reducing the computational load associated with estimating the attenuation properties of the canopy, yet still preserving the inhomogeneity of the canopy in a realistic fashion.
- 3.4.5 Trees are represented and stored in parametric form, and realized using procedures coded according to chosen tree species, and dependent upon chosen tree heights through allometric equations. Tree realizations are subsequently divided into scattering elements for the SAR imaging calculation.
- 3.4.6 A layer of understorey vegetation is accommodated at a simple level. It is homogeneous and of constant depth above local ground level. The layer is

comprised of small scattering elements, with uniform spatial and orientational distributions, yielding an azimuthally symmetric, homogeneous layer.

- 3.4.7 A two-scale model is adopted for the underlying ground surface. The DEM generated using user-supplied parameters provides the large-scale surface. This is divided into facets, taking their orientation from the large-scale surface, and assigned small-scale roughness for the scattering calculation.
- 3.4.8 Images are output in ground range and azimuth, and the backscattering alignment (BSA) convention is adopted.

3.5 Flow Chart for PolSARproSim Operation

3.5.1 **PolSARproSim** has an essentially linear design. Following input of the ASCII parameter file generated from PolSARpro **v2.0** the forest scene is generated: firstly by constructing a large scale ground surface, and then populating the forest stand area with trees and short vegetation. The biophysical properties of the trees are then used to generate a 3D map of attenuation. The attenuation map is used as a look-up table in the final stage: the calculation and output of simulated fully polarimetric, interferometric SAR imagery.

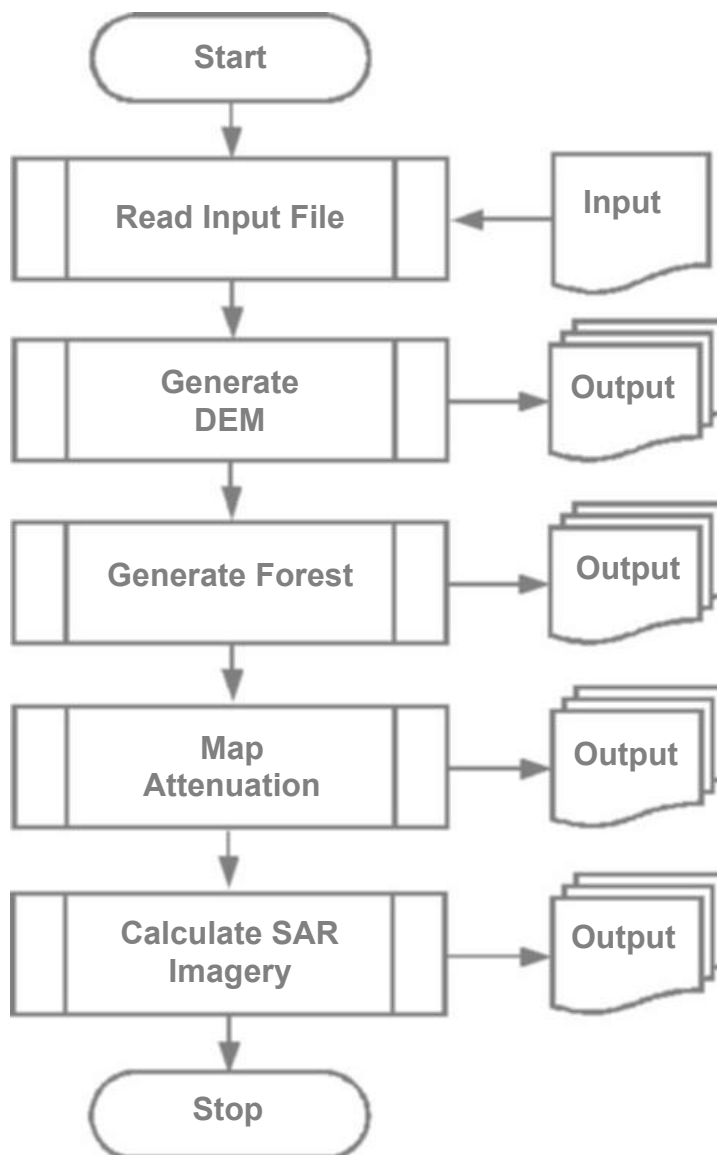


Figure 3.1 PolSARproSim flowchart

4 General Considerations

4.1 Terrain and Imaging Geometry

- 4.1.1 In the SAR simulation the imaging radar travels in the positive x -direction, with the antenna pointing portside. The SAR imaging plane is the global $x_g y_g$ -plane ($z_g = 0$). The image area lies between $-L_x/2.0 \leq x_g \leq L_x/2.0$ and $-L_y/2.0 \leq y_g \leq L_y/2.0$, where x_g is the azimuth coordinate, and y_g is the ground range coordinate, which increases away from the platform trajectory.
- 4.1.2 The forest stand occupies a circular area. In addition to the tree species (0-4), the mean height of the stand (metres), the stem density (trees/hectare) and the area of the forest stand (hectares) are supplied by the user. The scene area is calculated to comfortably accommodate the forest stand, taking into account layover and shadowing areas based on the user-supplied imaging geometry.
- 4.1.3 Slant range and global incidence angle are defined with reference to the (horizontal) SAR image plane. The platform trajectory is assumed uniform and parallel to the SAR image plane.
- 4.1.4 The large-scale ground surface, $g(x_g, y_g)$, is expressed as displacements about the mean terrain surface which is flat and tilted. The mean terrain surface has slope s_x in the x_g direction and s_y in the y_g direction. The ground surface height displacement about the mean terrain surface is periodic in x_g and y_g .
- 4.1.5 Imagery is output in the azimuth and ground range space, with far range appearing at the right of the images.

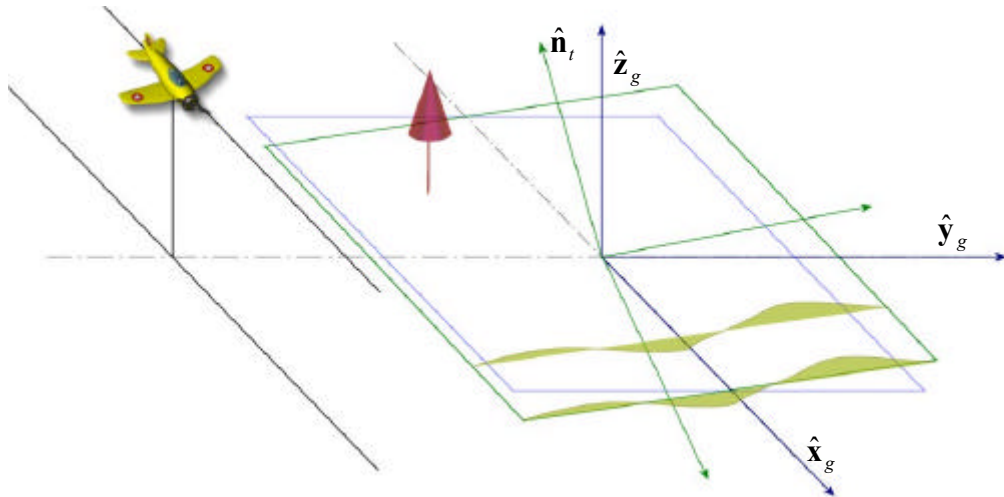


Figure 4.1 Terrain and Imaging Geometry

4.2 Input Parameters

4.2.1 The input parameter file is an ASCII text file with the three-letter extension “**sar**”, e.g. “**run001.sar**”. The following parameters are input to **PolSARproSim** from PolSARpro:

2	/* The number of requested tracks	*/
3192.533	/* Master slant range in metres	*/
20.0	/* Master incidence angle in degrees	*/
3194.2467	/* Slave slant range in metres	*/
20.084280	/* Slave incidence angle in degrees	*/
1.3	/* Centre frequency in GHz	*/
3.0	/* Azimuth resolution in metres	*/
1.026060	/* Slant range resolution in metres	*/
6	/* Ground model: 0 = smoothest ... 10 = roughest	*/
0.001	/* Ground slope in azimuth direction (dimensionless)	*/
0.002	/* Ground slope in ground range direction (dimensionless)	*/
222	/* Random number generator seed	*/
1	/* Tree species: 0 = HEDGE, 1,2,3 = PINE, 4 = DECIDUOUS	*/
16.5	/* Mean tree height in metres	*/
3927.0	/* Area of the forest stand in square metres	*/
550	/* Desired stand density in stems per hectare	*/
4	/* Ground moisture content model: 0 = dry ... 10 = wet	*/

Figure 4.2 An example of the ASCII input file format

4.2.2 Trees are one of essentially three varieties, a “hedge” which is a random collection of branches, “pine” trees or “deciduous” trees.

4.3 SAR Imaging Geometry

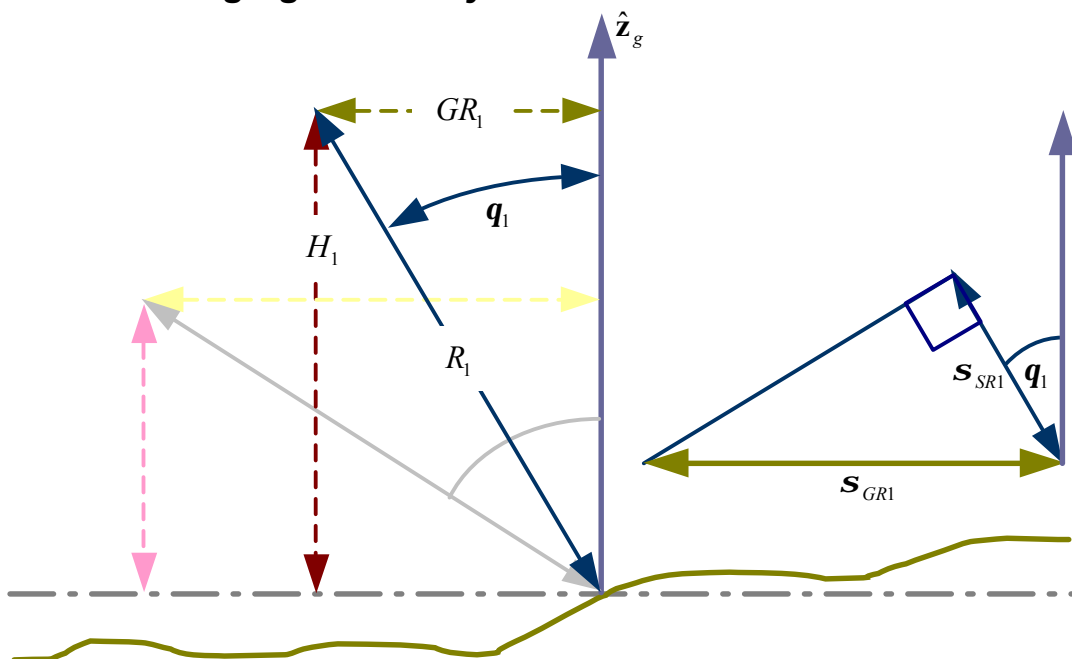


Figure 4.3 SAR Geometry

- 4.3.1 In the example of section 4.2 two tracks are specified with slant ranges and incidence angles of:

$$\begin{aligned} R_1 &= 3192.533 \text{ m.} & q_1 &= 20.0 \text{ deg.} \\ R_2 &= 3194.2467 \text{ m.} & q_2 &= 20.084280 \text{ deg.} \end{aligned}$$

- 4.3.2 The slant range resolution has been specified as

$$S_{SR} = 1.026060 \text{ m.}$$

- 4.3.3 which yields ground-range resolutions of

$$\begin{aligned} S_{GR1} &= S_{SR} / \sin(q_1) = 3.000 \text{ m.} \\ S_{GR2} &= S_{SR} / \sin(q_2) = 2.988 \text{ m.} \end{aligned}$$

- 4.3.4 The platform heights and ground ranges are therefore

$$\begin{aligned} H_1 &= R_1 \cos(q_1) = 3000.0 \text{ m.} \\ GR_1 &= R_1 \sin(q_1) = 1091.9 \text{ m.} \\ H_2 &= R_2 \cos(q_2) = 3000.0 \text{ m.} \\ GR_2 &= R_2 \sin(q_2) = 1096.9 \text{ m.} \end{aligned}$$

- 4.3.5 which correspond to horizontal and vertical baselines of

$$\begin{aligned} B_{hor} &= GR_2 - GR_1 = 5 \text{ m.} \\ B_{ver} &= H_2 - H_1 = 0 \text{ m.} \end{aligned}$$

4.4 SAR Image dimensions

- 4.4.1 The pixel sampling rate is defined by default to be 0.6667. Azimuth and slant range resolutions are user-defined as widths-at-half-height-power of the imaging point-spread-function (PSF). Ground-range resolution is slant-range resolution divided by the Sine of the incidence angle.

- 4.4.2 Mean tree crown radius is generated from user input tree species and tree height, and in the case of the hedge is equal to the radius of the forest stand.

- 4.4.3 The following length definitions are used to define the dimensions of the SAR image:

$$\begin{aligned} \text{Layover} &= \text{mean tree height} / \tan(\text{incidence angle}) \\ \text{Shadow} &= \text{mean tree height} \cdot \tan(\text{incidence angle}) \\ \text{Gap} &= 5 \cdot (\text{azimuth resolution} + \text{ground-range resolution}) \end{aligned}$$

- 4.4.4 The image area dimensions are then defined as azimuth:

$$L_x = 2 \cdot (\text{Stand radius} + \text{Gap}),$$

- 4.4.5 in the case of the hedge, and

$$L_x = 2 \cdot (\text{Stand radius} + \text{Gap} + \text{Mean crown radius}),$$

4.4.6 otherwise. In ground range:

$$Ly = Lx + Layover + Shadow.$$

4.4.7 To obtain the image dimensions in pixels the following algorithm is applied:

$$\begin{aligned} \text{deltax} &= 0.6667 \cdot \text{azimuth resolution}; \\ \text{deltay} &= 0.6667 \cdot \text{ground range resolution}; \\ nx &= (\text{int})(Lx / \text{deltax}) + 1; \\ nx &= 2 \cdot ((\text{int})(nx / 2)) + 1; \\ \text{deltax} &= Lx / nx; \\ ny &= (\text{int})(Ly / \text{deltay}) + 1; \\ ny &= 2 \cdot ((\text{int})(ny / 2)) + 1; \\ \text{deltay} &= Ly / ny; \end{aligned}$$

4.4.8 After which nx and ny are the image azimuth and range dimensions in pixels and deltax and deltay the dimensions in metres. In the current example:

$$\begin{aligned} \text{Layover} &= \text{mean tree height} / \tan(\text{incidence angle}) \\ &= 16.5 / \tan(20) \\ &= 45.333 \text{ m.} \\ \text{Shadow} &= \text{mean tree height} \cdot \tan(\text{incidence angle}) \\ &= 16.5 \cdot \tan(20) \\ &= 6.006 \text{ m.} \\ \text{Gap} &= 5 \cdot (\text{azimuth resolution} + \text{ground-range resolution}) \\ &= 5 \cdot (3 + 3) \\ &= 30 \text{ m.} \\ \text{Mean crown radius} &= 2.376 \text{ m. (not reported)} \\ Lx &= 2 \cdot (\text{Stand radius} + \text{Gap} + \text{Mean crown radius}) \\ &= 2 \cdot (35.36 + 30 + 2.38) \\ &= 135.5 \text{ m.} \\ Ly &= Lx + Layover + Shadow \\ &= 135.46 + 45.33 + 6.01 \\ &= 186.8 \text{ m.} \\ \text{deltax} &= 0.6667 \cdot \text{azimuth resolution} \\ &= 2.0 \text{ m.} \\ \text{deltay} &= 0.6667 \cdot \text{ground range resolution} \\ &= 2.0 \text{ m.} \\ nx &= (\text{int})(Lx / \text{deltax}) + 1 \\ &= (\text{int})(135.46 / 2.0) + 1 \\ &= 68 \\ nx &= 2 \cdot ((\text{int})(nx / 2)) + 1 \\ &= 2 \cdot ((\text{int})(68 / 2)) + 1 \\ &= 69 \\ \text{deltax} &= Lx / nx \\ &= 135.46 / 69 \\ &= 1.963 \text{ m.} \\ ny &= (\text{int})(Ly / \text{deltay}) + 1 \\ &= (\text{int})(186.8 / 2.0) + 1 \\ &= 94 \\ ny &= 2 \cdot ((\text{int})(94 / 2)) + 1 \\ &= 95 \\ \text{deltay} &= Ly / ny \\ &= 186.8 / 95 \\ &= 1.966 \text{ m.} \end{aligned}$$

5 DEM Generation

5.1 Introduction

- 5.1.1 This section describes the technique used for the generation of the large-scale digital elevation model. Arguments are given for the 2D case first, and then extended to 3D. The methods are inspired by those described in [42] (Tsang *et al.*, 2001)

5.2 Theory

- 5.2.1 The desired surface realization is described using a truncated Fourier series:

$$h(x) = \frac{1}{L} \sum_{n=-N}^N h_n \exp(i2\pi nx / L) \quad (5.2.1)$$

- 5.2.2 In (5.2.1) L is the length of the surface to be generated, and the surface is periodic with length L such that $h(x + nL) = h(x)$. Now writing $x' = 2\pi x / L$ we have

$$h(x') = \frac{1}{L} \sum_{n=-N}^N h_n \exp(inx'), \quad (5.2.2)$$

$$h(x' + 2\pi n) = h(x'), \text{ and} \quad (5.2.3)$$

$$h_n = \frac{L}{2\pi} \int_0^{2\pi} h(x') \exp(-inx') dx' \equiv H(k_n = 2\pi n / L) \quad (5.2.4)$$

- 5.2.3 The underlying surface correlation function is

$$c_h(s) = \int h(x)h(x+s)dx \quad (5.2.5)$$

- 5.2.4 Suppose we have a random function $f(x)$ with a very narrow correlation function. A realisation of such a function may be generated with a suitable random number generator. The Fourier transform (FT) of our desired function is

$$H(k) = W(k)F(k), \quad F(k) = FT[f(x)] \text{ etc.} \quad (5.2.6)$$

- 5.2.5 The desired correlation can then be written

$$\begin{aligned} c_h(s) &= \int h(x)h(x+s)dx \\ &= FT^{-1}[\|H(k)\|^2] \\ &= FT^{-1}[\|W(k)\|^2\|F(k)\|^2] \end{aligned} \quad (5.2.7)$$

- 5.2.6 In like manner the correlation of our random function is expressed as

$$c_f(s) = FT^{-1}[\|F(k)\|^2] \quad (5.2.8)$$

5.2.7 This correlation is very narrow, and in the limit of completely random noise we expect $c_f(s) \rightarrow \mathbf{d}(s)$, when we have, after suitable normalisation,

$$C_h(k) = FT[c_h(s)] = |W(k)|^2 \quad (5.2.9)$$

5.2.8 from which it follows that

$$H(k) = [C_h(k)]^{1/2} F(k) \quad (5.2.10)$$

5.2.9 or in the discrete model

$$H(k_m) = [C_h(k_m)]^{1/2} F(k_m), \quad (5.2.11a)$$

$$H(k_m = 2m\mathbf{p} / L) = \frac{L}{2\mathbf{p}} \int_0^{2\mathbf{p}} h(x') \exp(-imx') dx' = h_m \quad (5.2.11b)$$

5.2.10 Now the slopes on the mean flat terrain surface are s_x and s_y such that for any point in the SAR image plane $\mathbf{r} = (x, y, 0)$, the height of the mean flat surface is given as $xs_x + ys_y$. The mean terrain surface has surface normal vector:

$$\hat{\mathbf{n}}_t = (\hat{\mathbf{z}}_g - s_x \hat{\mathbf{x}}_g - s_y \hat{\mathbf{y}}_g) / (1 + s_x^2 + s_y^2)^{1/2} \quad (5.2.12)$$

5.2.11 which makes an angle \mathbf{q}_t with the global z-direction $\hat{\mathbf{z}}_g$ such that

$$\cos \mathbf{q}_t = \hat{\mathbf{n}}_t \cdot \hat{\mathbf{z}}_g = 1 / (1 + s_x^2 + s_y^2)^{1/2} \quad (5.2.13)$$

5.2.12 The displacements $h(x, y)$ calculated using the technique described in the following text are in the direction $\hat{\mathbf{n}}_t$ away from the mean surface at $\mathbf{t} = (x, y, xs_x + ys_y)$. To convert to the global frame make the simple *approximation* that the displacement h in the direction $\hat{\mathbf{n}}_t$ corresponds to a displacement in the global z-direction $\hat{\mathbf{z}}_g$ of $h \times (1 + s_x^2 + s_y^2)^{1/2}$. Thus the final height of the ground surface at azimuth x and ground range y is:

$$g(x, y) = xs_x + ys_y + h(x, y)(1 + s_x^2 + s_y^2)^{1/2} \quad (5.2.14)$$

5.3 DEM Generation Algorithm

5.3.1 The process of constructing the realisation of the surface proceeds as follows (now in 3D). In the frame of the local sloping terrain:

5.3.2 Create a random function $f(x, y)$.

5.3.3 Determine the coefficients,

$$F(k_m, k_n) = \int_0^{2p} \int_0^{2p} f(x', y') \exp(-imx') \exp(-iny') dx' dy' = f_{mn}, \quad (5.2.15)$$

5.3.4 where the lengths are increased by a factor $a = (1 + s_x^2 + s_y^2)^{1/2}$. The overall scaling can wait until the end. The integrals may be approximated as discrete sums for convenience:

$$F(k_{xm}, k_{yn}) \approx \sum_{i=0}^N \sum_{j=0}^N f(x'_i, y'_j) \exp(-imx'_i) \exp(-iny'_j) = f_{mn} \quad (5.2.16)$$

5.3.5 where $x'_i = i2p\Delta x / L_x$ and $y'_j = j2p\Delta y / L_y$, and all lengths are in the local terrain frame. Note here that $-N \leq m, n \leq N$ and $k_{xm} = 2mp / L_x$, whilst $k_{yn} = 2np / L_y$.

5.3.6 Determine the coefficients, $[C_h(k_{xm}, k_{yn})]^{1/2} = c_{mn}$. In our Gaussian correlation example below we have

$$[C_h(k_{xm}, k_{yn})]^{1/2} = \frac{l^2}{2} \exp(-k_{xm}^2 l^2 / 8) \exp(-k_{yn}^2 l^2 / 8) \quad (5.2.17)$$

5.3.7 Form the products, $h_{mn} = c_{mn} f_{mn}$.

5.3.8 Form the surface using,

$$h(x, y) = \sum_{m=-N}^N \sum_{n=-N}^N h_{mn} \exp(ik_{xm}x) \exp(ik_{yn}y) \quad (5.2.18)$$

5.3.9 Zero the mean height ($h(x, y) \rightarrow h(x, y) - \bar{h}$) and normalize the standard deviation to the desired value ($h(x, y) \rightarrow ah(x, y)$).

5.3.10 Finally the heights $h(x, y)$ may be interpreted as displacements about a tilted ground plane, and converted to global SAR frame (see section 2 above) displacements using

$$g(x_m, y_n) = x_m s_x + y_n s_y + h(x_m, y_m) (1 + s_x^2 + s_y^2)^{1/2}. \quad (5.2.19)$$

5.3.11 Note that with the choice:

$$c_h(s) = \exp(-s^2 / l^2) \quad (5.2.20)$$

5.3.12 and using

$$C_h(k) = \frac{1}{\sqrt{2p}} \int_{-\infty}^{\infty} c_h(s) \exp(iks) ds \quad (5.2.21)$$

5.3.13 we find

$$[C_h(k)]^{1/2} = \frac{l}{\sqrt{2}} \exp(-k^2 l^2 / 8) \quad (5.2.22)$$

5.3.14 Note that the algorithm yields a periodic set of displacements. To calculate the ground height outside of the SAR image area:

$$g(x + nL_x, y + mL_y) = g(x, y) + nL_x s_x + mL_y s_y \quad (5.2.23)$$

5.4 DEM Generation Summary

- 5.4.1 The following parameters are required to generate the large-scale DEM:
- 5.4.2 The circular forest stand area in square metres, A , under direct control of the user. The image area dimensions in metres, L_x and L_y , are generated from this area using knowledge of the imaging geometry and stand height.
- 5.4.3 Image dimensions in pixels, n_x and n_y , depending upon encoded pixel sampling rate, resulting from specified resolutions and image dimensions in metres.
- 5.4.4 The number of terms in Fourier expansion, N , specified by the programmer.
- 5.4.5 The terrain slopes, s_x and s_y , under control of the user.
- 5.4.6 Large scale surface correlation length in metres, l , recovered from mean tree separation.
- 5.4.7 Large-scale surface height standard deviation in metres, \mathbf{s}_l , recovered using a roughness model.
- 5.4.8 The user chooses between surface roughness on the basis of, “smooth” - 0, to “rough”-10. Roughness depends upon wavelength and incidence angle. Thus the user’s choice of surface roughness *value* (0-10) translates, into a numerical value for surface height standard deviation in metres.

5.5 Choice of Large-Scale Surface Roughness

- 5.5.1 Large-scale roughness is linked to power loss in the specularly reflected wave via the Rayleigh parameter [36] (Ogilvy, 1991) which scales the power of the specularly reflected wave according to

$$|R|^2 = \exp(-4k^2 \mathbf{s}_l^2 \cos^2 \mathbf{q}) \quad (5.5.1)$$

- 5.5.2 Here $\mathbf{s}_l = \mathbf{s}_l + \mathbf{s}_s$ is the total (large-scale + small-scale) roughness. The user enters a roughness number $0 \leq r \leq 10$ from which the power reduction on the reflected wave is determined according to

$$10 \log_{10}(|R|^2) = \text{min RdB} - (r/10)(\text{min RdB} - \text{max RdB}) \quad (5.5.2)$$

- 5.5.3 where minRdB and maxRdB are programmer assigned constants. The large-scale roughness is then assigned according to

$$\mathbf{s}_l = \sqrt{-\ln(|R|^2) / (2k \cos \mathbf{q})} - \mathbf{s}_s \quad (5.5.3)$$

- 5.5.4 The large-scale correlation length is always chosen as 3 times the mean tree crown radius of a pine tree at the requested tree height. The choice of small-

scale roughness and correlation length is discussed in the section on SAR image calculation.

6 Tree Location Map Generation

6.1 Introduction

- 6.1.1 This section describes the generation of the tree location map. The tree location map consists of a list of azimuth and ground range coordinates for the base point of each tree. This point is the stem base for a tree with a single stem.
- 6.1.2 For each coordinate pair there is an associated tree height. The tree height is drawn from a normal distribution. The user specifies directly the mean tree height in metres. The tree height standard deviation is set to 5% of the mean value.
- 6.1.3 The tree height is a fundamental quantity. All allometric equations are functions of tree species (specified by the user) and tree height. Thus the tree global crown radius (see later definition of the Tree "object"), is calculated from tree height using a species-specific allometric equation. This crown radius is used in the generation of tree locations.
- 6.1.4 The process of tree location map generation begins by determining the number of trees in the scene, and then initializing them in a regular pattern, and realizing their heights and global crown radii. The trees are subsequently "shuffled" around in random, collision-avoiding walks using Monte Carlo techniques, to reach a more realistic distribution of tree positions.

6.2 Algorithm Details

- 6.2.1 The user has provided the area dimensions, tree species, and mean height of the forest stand. From the last two quantities is derived the mean crown radius using the encoded allometric equation.
- 6.2.2 Given the area and the mean crown radius the maximum number of trees that might be expected within that area if they are close-packed in 2-dimensions (with discs of mean crown radius occupying a fraction 0.907 of the total area) is calculated. Trees are permitted to have crowns that overlap by as much as 11%.
- 6.2.3 The user specifies stand density in stems/hectare. If the requested stand density is greater than the calculated maximum by a certain amount the actual stand density is the smaller of the two, otherwise the actual stand density is the requested density.
- 6.2.4 From the actual stem density in stems/hectare the stem line density in stems/100m is determined as the square root of the stem density. Initially trees are to be located on grid coordinates, and the grid dimensions are now recovered using the area dimensions and the stem line density. Note that since the final number of trees is the product of two integers, so the requested stem density is not matched precisely.

- 6.2.5 Having determined the grid dimensions the trees are located on grid points with alternate lines shifted by half a grid spacing to offset the initial tree positions. Tree locations are then "shuffled" using an annealing Monte Carlo algorithm (see e.g. [43] (Binder (Ed.), 1979)).
- 6.2.6 The shuffling is controlled using the crown radii and a cost function, which rises steeply as the trees approach a separation within their combined radii, and has a small attractive effect for greater tree separations. The technique yields realistic, non-uniform distributions of tree locations, which appear quite natural.
- 6.2.7 The shuffling treats the image area as periodic, so that trees shuffling out of the area to the right, shuffle into the area from the left, and similarly from top to bottom, and vice versa. Exploiting periodicity permits the expansion of the simulated area, whilst preserving a natural tree separation distribution, and avoiding trees that are too close together.
- 6.2.8 Finally, from the full list of tree positions, a circular area is excised that corresponds to the forest stand area requested by the user. This circular area is offset slightly in ground-range in order to accommodate the extent of layover. The tree locations, heights and crown radii are output to a text file.
- 6.2.9 The scene geometry accommodates layover and shadow regions as calculated previously:

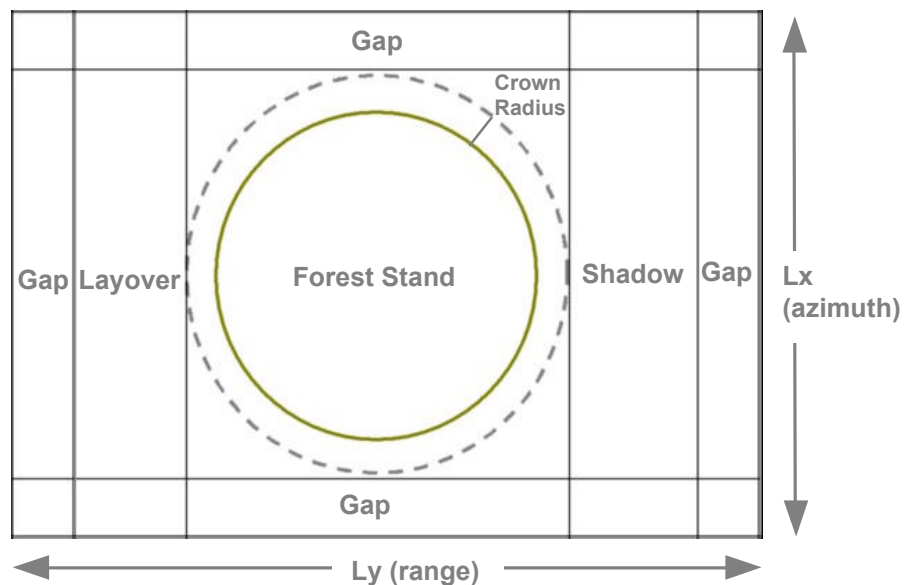


Figure 6.1 Scene geometry

6.3 *Tree Location Map Summary*

- 6.3.1 The following parameters are required to generate the tree location map: the forest stand area, the mean tree height in metres, and the requested stand density. In addition the allometric equation relating tree mean crown radius to tree height and species is also required.

6.4 *Special Note on the HEDGE Option*

- 6.4.1 In keeping with the previous version of **PoISARPro**, it is possible for the user to specify a single HEDGE model of the canopy, rather than a forest stand. In this case no shuffling is required. Choosing the HEDGE option results in a single, cylindrical tree-crown at scene center, with no stems, primary or secondary branches, but only tertiary branches and leaves. Details of this option are given in later sections.

7 Tree Species and Architecture

7.1 Introduction

- 7.1.1 To complete the description of the forest stand we require a description of the tree architectures. Each tree, when realized, appears unique: with its own arrangement of stem, primary and secondary branches, and a crown volume filled with tertiary branch elements and leaves.
- 7.1.2 The description of the tree then resides in the procedures and algorithms used to generate these realizations. A broad description of these algorithms, and the structures upon which they operate, is given in the following sections. Actual parameter values controlling their operation have been refined during the development process to ensure that predicted SAR backscattering coefficients are within observational limits.
- 7.1.3 There are a variety of species options in the initial version of **PolSARproSim**. These are the hedge model (HEDGE option) and trees chosen to resemble pines (PINE001/2/3 option) or broad-leaved trees (DECIDUOUS001 option). Future versions of the software may include additional options.

7.2 Trees

- 7.2.1 Although programming in C it is useful to think, in object-oriented terms, of trees represented in the software as objects, and in practice trees are represented as structures.
- 7.2.2 The definition of a tree record includes the species, a vector location, **base**, and the tree height and radius in metres. These quantities are assigned and used in the tree shuffling procedure.
- 7.2.3 In addition the record contains lists of stems, primary and secondary branch objects, whose definitions are considered shortly. The definition of a tree record also contains a list of crown volumes occupied by tertiary branches and leaves (or needles in the case of the PINE001/2/3 option).
- 7.2.4 For the HEDGE option there is only a single tree, with a single crown represented by a finite cylinder; its axis vertical in the global frame, and truncated by planes parallel to the mean ground surface. The Stem_List, Primary_Branch_List and Secondary_Branch_List of a HEDGE option Tree are empty, whilst the crown list has a single entry. Crowns, Branches and Cylinders are discussed in due course. The hedge is comprised of both deciduous leaves and branches.
- 7.2.5 Option PINE001 resembles a pine tree in that it has a single stem, which is very straight, and primary branches which radiate from the central stem in layers. These trees have two crowns: an upper living crown, and a lower dry crown without green vegetation. Primary branch structure is predominantly

radial, with branch angle varying with height. The living crowns of PINE001 option trees are occupied by tertiary branches and needles. Other options for pine trees having either conical crown shapes (PINE002) or mixed crown shapes (PINE003) are also implemented.

- 7.2.6 Option DECIDUOUS001 is much broader than the pine model and has stems which are not straight and which lean considerably. These trees are created by defining a stem with a large crown. Primary branches are then created from the stem to points within the crown. Secondary branches are then created from primaries and associated crowns. The crowns of DECIDUOUS001 trees are also occupied by tertiary branches and deciduous leaves.
- 7.2.7 Delivery of HEDGE and one of PINE001, PINE002, PINE003 or DECIDUOUS001 is included in the present contract.

7.3 Branches

- 7.3.1 Branches are represented in the computer as curved, tapering cylinders. These are converted into a series of short, straight cylindrical sections for the purposes of the scattering calculation.
- 7.3.2 The basic branch shape is defined in terms of the location of the centre of the branch:

$$\mathbf{b}(t) = \mathbf{b}_0 + l \left[t \hat{\mathbf{z}}_0 + \frac{d_p}{2(1-d_p^2)^{1/2}} t^2 \hat{\mathbf{p}} + \mathbf{c}(t) \right] \quad (7.3.1)$$

- 7.3.3 In (7.3.1) l is the “straight” branch length, and t is a parametric value, which is zero at the start of the branch and unity at the tip of the branch. The unit vector $\hat{\mathbf{z}}_0$ defines the initial direction of the branch. In the absence of curvature, $\mathbf{c}(t)$, the branch is straight and maintains its initial direction and $\mathbf{b}(t) = \mathbf{b}_0 + lt\hat{\mathbf{z}}_0$.

- 7.3.4 The branch may bend towards a specific direction, $\hat{\mathbf{p}}$, to mimic the natural tendency of branches to grow towards the light or to sag under the effects of gravity. For example see [44, 45] (Weber and Penn, 1995, Lintermann and Deussen, 1999).

- 7.3.5 A quadratic form for the bending function is adopted such that in the absence of curvature the direction of the branch is

$$\hat{\mathbf{z}}(t) = \frac{(1-d_p^2)^{1/2} \hat{\mathbf{z}}_0 + t d_p \hat{\mathbf{p}}}{[1+(t^2-1)d_p^2]^{1/2}} \quad (7.3.2)$$

- 7.3.6 where $0 \leq d_p < 1$ is a “bending factor” (species and branching order dependent) controlling the amount of bending towards the $\hat{\mathbf{p}}$ direction.
- 7.3.7 The curvature function is the sum of cosines with randomized wavelengths and phases that mimic the irregular shapes of real branches.
- 7.3.8 Parameter values are drawn from species-specific distributions. For example the start radius depends upon the radius of the parent branch at the branching point etc. The branch radius decays linearly from the start value to the end value with the parameter, t .
- 7.3.9 Branches are subdivided into segments (Cylinders) in the code for drawing and scattering calculations, and the branch equation is used to determine the Cylinder properties for each branch segment.

7.4 Crowns

- 7.4.1 All crown objects relate to volumes of type cylinder, cone or truncated ellipsoid. Crowns are populated by leaves and twigs (tertiary branches) and these require dimensions, permittivities, orientations and volume fractions. These are all hardwired by species, so that we need only define the crown type, which is defined by the species of the associated Tree (crowns never appearing in isolation).
- 7.4.2 Crowns are truncated by bounding planes. For example in the case of the HEDGE, the crown is a vertical cylinder terminated at each end by a flat surface parallel to the mean sloping terrain. A conical crown is terminated at the wide end by a similar plane surface, and an spheroidal crown is truncated, again using a similar surface.
- 7.4.3 Since Crown bounding surfaces are always taken parallel to the mean sloping terrain and known to pass through specific points they are not stored explicitly as part of Crown structures. Instead Crown structures store the slopes of the bounding planes, and Plane objects are constructed from Crown field data as required.

It is necessary to understand the intersection of rays with planar and crown surfaces in order to implement the estimation of attenuation when performing the SAR calculation. So in addition to a planar surface a Ray object is also defined.
- 7.4.4 The details of Ray-Crown and Ray-Plane intersections are given in the Appendix.

7.5 Realization of Trees

- 7.5.1 The HEDGE, as in the previous data included with **PolSARPro** v1.0, has no stems, primary or secondary branches, and consists of a single cylindrical living crown centred at the origin. The base of the cylinder is at the local ground height.
- 7.5.2 Tertiary elements only realized on demand for the SAR calculation, and are otherwise not called into existence. So the creation of the Tree record for the HEDGE is particularly straightforward.
- 7.5.3 The PINE001 model has a single, near-vertical stem. There are two crowns: an upper living crown with an SPHEROIDAL shape, truncated in half, and a lower dry crown, with a CYLINDRICAL shape having the same radius as the upper crown maximum radius. PINE001 trees have terminating planes parallel with the mean sloping terrain, and this has consequences for matching the radius of the cylindrical dry crown layer to the upper living crown spheroid.
- 7.5.4 A DECIDUOUS001 model has a single, highly curved stem and one living crown. Primaries are large but few in number, almost like stems themselves, and generated using the large global crown. Secondaries are created starting from the primary and reaching the crown surface. The crown is populated with tertiary elements as required. The crown is spheroidal.
- 7.5.5 Together with species definitions, ground generation, tree location generation and short vegetation description, this completes the model of the forest.

7.6 Generating Stems and Branches

- 7.6.1 The definition of a branch is based around an equation describing the curved branch centre. This equation has the form (repeated here for convenience):

$$\mathbf{b}(t) = \mathbf{b}_0 + l \left[t \hat{\mathbf{z}}_0 + \frac{d_p}{2(1-d_p^2)^{1/2}} t^2 \hat{\mathbf{p}} + \mathbf{c}(t) \right] \quad (7.6.1)$$

- 7.6.2 where the non-curved “direction” of the branch is

$$\hat{\mathbf{z}}(t) = \frac{(1-d_p^2)^{1/2} \hat{\mathbf{z}}_0 + t d_p \hat{\mathbf{p}}}{[1 + (t^2 - 1) d_p^2]^{1/2}} \quad (7.6.2)$$

- 7.6.3 The curvature component is a correction to the central branch position, and parameter values are chosen appropriately (species and branching order dependencies are involved for the wavelengths and overall scaling, but the phase angles are uniformly random on $[0, 2\pi]$).
- 7.6.4 To find the remaining parameter, l , specify the branch termination on the crown volume surface, i.e.

$$\mathbf{b}(t=1) = \mathbf{b}_0 + l \left[\hat{\mathbf{z}}_0 + \frac{d_p}{2(1-d_p^2)^{1/2}} \hat{\mathbf{p}} \right] = \mathbf{b}_0 + l [\hat{\mathbf{z}}_0 + f_p \hat{\mathbf{p}}] \quad (7.6.3)$$

- 7.6.5 This point is found by starting at the point \mathbf{b}_0 , and searching for the intersection of a ray with the crown volume in the direction $\hat{\mathbf{a}} = (\hat{\mathbf{z}}_0 + f_p \hat{\mathbf{p}}) / |\hat{\mathbf{z}}_0 + f_p \hat{\mathbf{p}}|$ to find a point, \mathbf{b}_1 , from which the “straight length” l may be recovered as

$$l = \frac{(\mathbf{b}_1 - \mathbf{b}_0) \cdot \hat{\mathbf{z}}_0}{[1 + f_p (\hat{\mathbf{p}} \cdot \hat{\mathbf{z}}_0)]} \quad f_p = \frac{d_p}{2(1 - d_p^2)^{1/2}} \quad (7.6.4)$$

- 7.6.6 We specify the base, initial direction and bending vectors at the outset, then the branch length is found by seeking the intersection of the ray with the crown surface.
- 7.6.7 The same process is adopted for stems, primaries and secondary branches. Thus, given the appropriate rules, and techniques for finding ray intersections with crown volume surfaces, we have all that is necessary to construct the Trees. During the creation of secondary branches temporary sub-crowns are created for each primary branch.
- 7.6.8 The algorithms for finding ray intersections with different geometric objects are given in the Appendix.



Figure 7.1 Examples of “pine” tree architectures realised using the techniques discussed in the text.

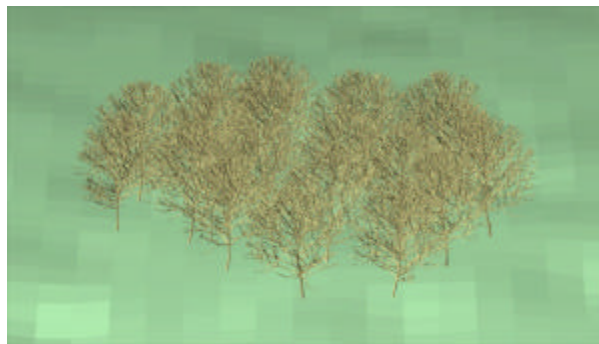


Figure 7.2 Examples of “deciduous” tree architectures realised using the techniques discussed in the text.

8 Interferometric SAR Image Calculation

8.1 Introduction

- 8.1.1 It might appear to be most efficient to calculate both images at the same time, using a "dual-antenna" approach rather than a "repeat-pass" approach. This would have the advantage of only requiring realization of the forest a single time. However there are a number of overheads associated with this idea.
- 8.1.2 The first and most obvious is the memory requirement. Not only is this doubled for the images themselves but other structures, such as the attenuation grid, to be discussed in the following sections, must be reproduced.
- 8.1.3 Nor is there a great saving in computational load. Whilst the "repeat-pass" method doubles the realization cost, and requires care and attention to exact reproduction of the scene, this computational load is not a critical factor. From experience the heaviest computational load arises in the calculation of effective permittivity by voxel, scattering amplitude calculations using sophisticated models for cylinder scattering, and determination of focus points, particularly for the ground-volume interactions. All of these overheads are present in both the "dual-antenna" and "repeat-pass" approaches.
- 8.1.4 Thus the approach to be adopted is "repeat-pass", which in some respects presents a less complex coding challenge, with a greater concomitant potential for success. This involves calling a single routine twice, each time with a slightly different imaging geometry.
- 8.1.5 The SAR image calculation phase may be broken down into stages. The first of these is the calculation of canopy tree crown and understorey permittivities. Crowns are taken to have the same mean permittivity. Thus tree crown effective permittivities are calculated in the Foldy-Lax approximation [38] by averaging the forward scattering amplitudes of their constituent elements. The same approach is adopted for the short vegetation layer, which is also taken to be homogeneous and isotropic, and to have constant depth above local ground height.
- 8.1.6 The next stage is to construct attenuation grids, which supply look-up tables for attenuation by spatial location. The attenuation grids are used when calculating scattering to provide approximate estimates of attenuation by location in a very efficient way that enhances the simulation performance, yet still maintain the effects of the inhomogeneity of the tree crown distribution.
- 8.1.7 Having determined the attenuation grids the next stage is the calculation of SAR images. This starts with the direct-ground (DG) calculation, which employs the techniques described in [10] (M L Williams, 2006) and which are reproduced in the following sections. Essentially the ground surface is divided into numerous facets, and these are assigned complex scattering amplitudes, and focused in the image one after the other, each being scaled by the attenuation estimate for its location in the scene.

- 8.1.8 The next calculations, direct-volume (DV) and ground-surface-volume (SV) for the short vegetation layer are conducted together to reduce computational load. The technique uses the hybrid stochastic-deterministic approach described in [10]. A subset of plant elements is realized, and their scattering amplitudes scaled to yield the backscattering coefficient anticipated by the full sample. The number of realizations per resolution cell is sufficient to provide fully-developed speckle, and the actual realizations are preserved for the second interferometric SAR image.
- 8.1.9 The final calculation is conducted for the forest of trees. Each tree location is addressed in turn. A unique distribution of stem, primary and secondary branches is created and subdivided into short cylindrical elements. Both direct-forest (DF) and ground-surface-forest (SF) terms are calculated for these elements. Finally the hybrid technique adopted for short vegetation is adopted for scattering from the smaller tree crown elements of leaves, twigs and pine needles.
- 8.1.10 After writing out the first set of SAR imagery to an appropriately named file, the whole process is repeated for the repeat-pass scenario, taking care to preserve random number sequences where appropriate and ensure consistency of scene realization.
- 8.1.11 The full process is described in greater detail in the following sections.

8.2 Representation of the SAR Image

- 8.2.1 The forward SAR model employs a representation of the SAR image as a coherent (phase-preserving) transform of a radar reflectivity function. This model is derived in [10], and the derivation is repeated here for convenience.
- 8.2.2 The SAR image is taken to be formed using transmission and reception of regular pulses of the form:

$$\mathbf{p}(t) = \int_{-\infty}^{\infty} \hat{p}(\mathbf{w}) \exp(-i\mathbf{w}t) d\mathbf{w} \hat{\mathbf{e}} = p(t) \hat{\mathbf{e}} \quad (8.2.1)$$

- 8.2.3 The received signal when the platform is at “position” x is

$$\mathbf{s}(t, x) = \int_{-\infty}^{\infty} \underline{\mathbf{B}}(\mathbf{w}, x) \cdot \hat{\mathbf{e}}(x) \hat{p}(\mathbf{w}) \exp(-i\mathbf{w}t) d\mathbf{w}, \quad (8.2.2)$$

- 8.2.4 i.e. the total return from the illuminated scene, where

$$\underline{\mathbf{B}}(\mathbf{w}, x) = \int \underline{\mathbf{F}}(\mathbf{w}, x, \mathbf{s}) \exp(i\mathbf{w}2r(x, \mathbf{s})/c) d\mathbf{s} \quad (8.2.3)$$

- 8.2.5 and $\underline{\mathbf{F}}(\mathbf{w}, x, \mathbf{s})$ is the reflectivity density at the point \mathbf{s} with range $r(x, \mathbf{s})$. The correlation of the received signal with the return anticipated from a delayed pulse is:

$$\begin{aligned} \underline{?}(t, y) &= \iint \underline{\mathbf{s}}(\underline{\mathbf{t}}, x) \underline{p}^*(\underline{\mathbf{t}} - \underline{\mathbf{t}}'(x, t, y)) d\underline{\mathbf{t}} dx \\ &= \iint \underline{\mathbf{s}}(\underline{\mathbf{t}}, x) \underline{p}^*(\underline{\mathbf{t}} - 2|\underline{\mathbf{r}}_p(x) - \underline{\mathbf{r}}(t, y)|/c) d\underline{\mathbf{t}} dx \end{aligned} \quad (8.2.4)$$

8.2.6 Here $\underline{\mathbf{r}}_p(x)$ is the platform location at x , and $\underline{\mathbf{r}}(t, y)$ is the location of the scattering centre at the point of interest in the image. Using the definition of the pulse in terms of its Fourier spectrum

$$\underline{p}^*(\underline{\mathbf{t}} - \underline{\mathbf{t}}') = \int_{-\infty}^{\infty} \hat{\underline{p}}^*(\underline{\mathbf{w}}') \exp(i\underline{\mathbf{w}}'(\underline{\mathbf{t}} - \underline{\mathbf{t}}')) d\underline{\mathbf{w}}' \quad (8.2.5)$$

8.2.7 in the expression for the correlated image leads to

$$\underline{?}(t, y) = \int \int_{-\infty}^{\infty} \underline{\mathbf{B}}(\underline{\mathbf{w}}, x) |\hat{\underline{p}}(\underline{\mathbf{w}})|^2 \exp(-i\underline{\mathbf{w}}\underline{\mathbf{t}}'(x, t, y)) d\underline{\mathbf{w}} dx \quad (8.2.6)$$

8.2.8 Substituting for $\underline{\mathbf{B}}$ the SAR image function is:

$$\underline{?}(t, y) = \int \int \int_{-\infty}^{\infty} [\underline{\mathbf{F}}(\underline{\mathbf{w}}, x, \underline{\mathbf{s}}) |\hat{\underline{p}}(\underline{\mathbf{w}})|^2 e^{i\underline{\mathbf{w}}[2r(x, \underline{\mathbf{s}})/c - \underline{\mathbf{t}}'(x, t, y)]}] d\underline{\mathbf{w}} dx d\underline{\mathbf{s}} \quad (8.2.7)$$

8.2.9 The approximation of constant reflectivity across the SAR bandwidth and aperture is adopted so that

$$\underline{?}(t, y) = \int \underline{\mathbf{F}}(\underline{\mathbf{s}}) \hat{\underline{Q}}(t - r(\underline{\mathbf{s}}), y - x) d\underline{\mathbf{s}}, \quad (8.2.8)$$

8.2.10 and

$$\hat{\underline{Q}} = \int \int_{-\infty}^{\infty} |\hat{\underline{p}}(\underline{\mathbf{w}})|^2 \exp(i\underline{\mathbf{w}}[2r(x, \underline{\mathbf{s}})/c - \underline{\mathbf{t}}'(x, t, y)]) d\underline{\mathbf{w}} dx \quad (8.2.9)$$

8.2.11 is the system impulse response or point spread function. This quantity is approximated in the simulation using a Gaussian function product in azimuth and ground range, with appropriate range phase.

8.2.12 This result is valid for direct scattering from a surface or volume scattering, and higher orders of scattering involving surface-surface, or volume-surface, or surface-volume-surface etc. The point, $\underline{\mathbf{s}}$, need not be a location either in or on a scattering object, but rather in general it is an *effective* scattering centre associated with the reflectivity determined from interacting scene elements that are spatially separated: examples follow in the next sections.

8.2.13 A discrete approximation is employed:

$$\underline{\mathbf{I}}(r', x') = \sum_n \underline{\mathbf{F}}_n \hat{\underline{Q}}(r' - r(\underline{\mathbf{s}}_n), x' - x(\underline{\mathbf{s}}_n)) \quad (8.2.10)$$

- 8.2.14 where the polarimetric scattering amplitude, $\underline{\mathbf{F}}_n$, associated with the n^{th} scattering event, arising from one or more elements of the scene, and incorporating attenuation, has an *effective* scattering centre, \mathbf{s}_n .
- 8.2.15 SAR image prediction using this model proceeds as follows: describe the scene geometrically and physically, as described in the preceding sections, then divide the scene into small (relative to system resolution) elements. Interrogate the scene and determine scattering events (divided by class), calculating their polarimetric scattering amplitudes, and associated *effective* scattering centres. Sum their contributions *coherently* into the image accumulator, $\underline{\mathbf{I}}(r', x')$.
- 8.2.16 Whilst simple in concept the procedure entails a heavy computational load mitigated only by the use of approximations that preserve important features of the SAR imagery such as clutter distribution, shadowing and interferometric coherence.

8.3 Modelling Attenuation

- 8.3.1 This requires estimation of the complex permittivity of the random media comprising the tree crowns and the short vegetation. In previous work of this kind the technique was to divide the canopy into voxels and to identify the material occupying those voxels. The scattering properties of occupying vegetation elements were used to estimate the mean, or effective permittivity in each voxel. Then during the SAR calculation, for each scattering event a list was built indicating through which voxels the broadside ray passed for that event, and the attenuation due to each voxel was calculated and accumulated into the scattering amplitude.
- 8.3.2 This process is somewhat inefficient and therefore unsuitable to the present task. The intention is to adopt a new, more efficient method. The first stage is to estimate an effective permittivity for both the short vegetation layer, and the tree crowns. Each crown is given the same mean permittivity. The permittivity estimate is determined by integrating the forward scattering amplitudes of plant elements and interpreting them as effective polarisabilities. Thus the approximation corresponds to the Foldy-Lax model [38], which is used widely and appropriate for the wavelengths under consideration.
- 8.3.3 Having determined the mean dielectric properties of crowns and short vegetation a 3D grid of points is generated to sample the attenuation function. One grid is required for the incident and scattering directions, and another for the ground reflection direction. For each grid point the broadside ray paths are determined and the attenuation associated with the path determined by finding ray intersections with the boundaries of the understorey layer and the crowns. Transmission coefficients are generally close to unity and are not required. In reality of course our crown boundary is completely artificial, as trees do not have well-defined crown volumes, which in itself is good reason for omitting transmission boundary effects.

- 8.3.4 During the SAR image calculation the grid is used as a look-up table for attenuating scattering amplitudes. A scattering amplitude is assigned the same polarimetric attenuation as that associated with the nearest grid point to the scatterer centre. This provides efficiency and preserves the effects of inhomogeneity.

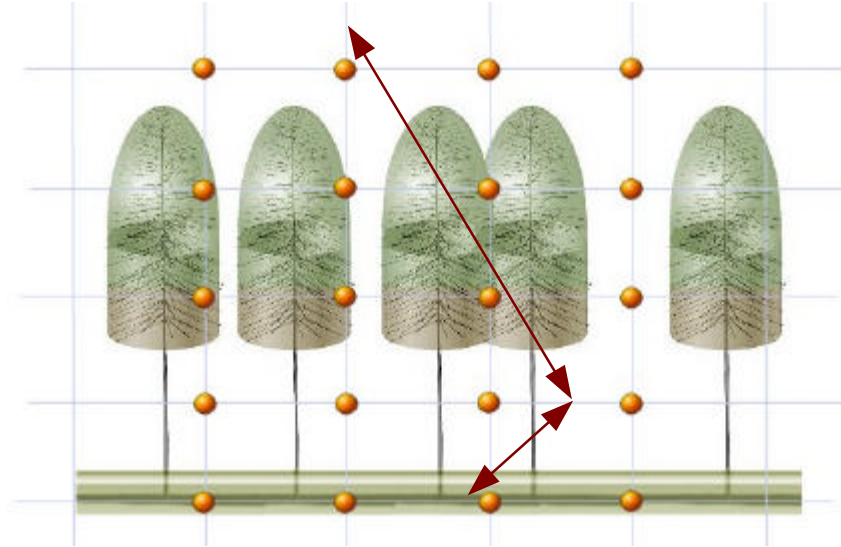


Figure 8.1 Mapping of attenuation into the 3D space occupied by the forest canopy. Direct and reflected ray paths are determined for each grid point. The passage of each ray through crowns and short vegetation is used to determine the attenuation associated with each path.

8.4 Direct-Ground (DG) SAR Image

- 8.4.1 The ground surface is divided into flat, rough facets, derived from the large-scale DEM. In principle each facet has a unique realisation of surface roughness drawn from an underlying statistical distribution. The polarimetric scattering amplitude of each facet is therefore unique: the variation leading to speckle in the DG term under the right conditions. A fully deterministic approach to the calculation of DG terms is computationally prohibitive. Thus facet scattering amplitudes are calculated using the covariance matrix associated with the underlying surface scattering model calculated in the local frame of the facet.

- 8.4.2 In past work [10] each facet was assigned a complex, polarimetric scattering amplitude drawn from the multivariate Gaussian distribution:

$$p(\mathbf{S}) = \exp(-\mathbf{S}^* \underline{\mathbf{C}}^{-1} \mathbf{S}) / (\mathbf{p}^3 \det \underline{\mathbf{C}}) \quad (8.4.1)$$

- 8.4.3 sampled using Monte Carlo (MC) techniques.
- 8.4.4 The model employed is two-scale, with the small perturbation model (SPM) used to model the small-scale response. The copolar channels are perfectly correlated in the SPM, and even with large-scale roughness effects this can lead to unrealistically low polarimetric entropy in the DG term. Thus in

practice the covariance matrix approach is adopted using a high (0.95) HH-VV correlation, although this requires careful sampling.

- 8.4.5 Sampling eqn. (8.4.1) at high HH-VV coherence is problematic, and an alternative approach has been adopted for this study. Since in the SPM HH and VV are perfectly correlated, so we may choose a single, local scattering amplitude factor for each facet, using a single complex gaussian distribution. To afford a more realistic polarimetric entropy, the local scattering amplitude matrix recovered this way is rotated about the radar line-of-sight by a random angle chosen from a uniform distribution the extent of which is designed to achieve the desired HH-VV coherence in the local frame of the facet [37] (Hajnsek *et al.*, 2003). The final local scattering amplitude is then converted into the radar frame.
- 8.4.6 The hybrid deterministic-stochastic technique is made to preserve interferometric coherence by preserving the random number sequence employed in the MC sampling. In practice any change in incidence angle, however slight, may alter the course of the MC sampling on some facets as the local facet incidence alters the local mean RCS and covariance. This can have a small effect upon coherence for the occasional image pixel. This effect may be minimised by preserving the scaled facet scattering amplitude factors between tracks of the interferometric baseline. Even without this precaution the technique yields high, mean ground coherence as desired.

8.5 Choice of Small-Scale Parameters

- 8.5.1 DG facet scattering amplitudes are calculated in the small perturbation model (SPM) as recorded in [36] (Ogilvy, 1991). Surfaces are taken to be Gaussian correlated and the choice of surface roughness and correlation length are recovered using the users choice of roughness model in the following way.
- 8.5.2 A choice is first made for the surface roughness which complies with the limit of validity of the SPM by assigning

$$\mathbf{s}_s = \mathbf{a} / (k \cos \mathbf{q}) \quad (8.5.1)$$

- 8.5.3 where $\mathbf{a} \ll 1$ is a constant of the program. Given a roughness the correlation length corresponding to maximum backscattering coefficient is found as

$$\hat{\mathbf{l}}_s = 1 / (k \sin \mathbf{q}) \quad (8.5.2)$$

- 8.5.4 From which is recovered the maximum possible SPM ground brightness at the current incidence, wavelength and roughness, $\hat{\mathbf{S}}_{hh}^0$. The default ground brightness is chosen according to frequency, f , using $f_p = 0.4333$ GHz, $f_L = 1.3000$ GHz, $\mathbf{df} = (f - f_p)/(f_L - f_p)$ where $\mathbf{df} = 0$ if $f < f_p$ and $\mathbf{df} = 1$ if $f > f_L$. Then using $\mathbf{S}_{hhL45}^o = -28\text{dB}$ and $\mathbf{S}_{hhP45}^o = -38\text{dB}$, $\mathbf{S}_{hh}^o = \mathbf{df} \times \mathbf{S}_{hhL45}^o + (1 - \mathbf{df}) \times \mathbf{S}_{hhP45}^o$.
- 8.5.5 Now the user defined surface roughness parameter ($0 \leq r \leq 10$) is used to adjust the desired ground brightness according to $\mathbf{S}_{hh}^o = \mathbf{S}_{hh}^o + \Delta_{hh}^o \times (r - 5)/5$, $\Delta_{hh}^o = 3\text{dB}$.
- 8.5.6 Now if the desired backscatter is greater than the maximum possible, then the correlation length chosen is that corresponding to maximum backscatter, i.e. $\mathbf{I}_s = \hat{\mathbf{I}}_s$, otherwise the correlation length is found that yields the desired backscattering coefficient by finding the solution using the Newton-Raphson algorithm.

8.6 The DG Imaging Algorithm

- 8.6.1 The model for surface scattering is two-scale. The large-scale DEM is divided into triangular facets, with at least 10 per resolution cell to ensure fully-developed speckle in the final image. Each facet has its own orientation and area determined by its location on the large-scale surface, and at the small-scale each facet is presumed to have its own unique realization of roughness, taken from a global, Gaussian roughness model.
- 8.6.2 The facet orientation, area and small-scale roughness are used to determine the scattering amplitude of the surface facet in the global frame. The facet centre position is used to determine the point of focus of the facet in the SAR image plane (the global $z = 0$ plane), and the interferometric phase of the facet contribution to the DG image. The system point-spread-function (PSF) is used to focus the facet return in the image, and assumes that the facet dimensions are much smaller than resolutions, which they are.
- 8.6.3 We first note that in the Bragg model, or first order small perturbation model (SPM), in the local frame of the facet the cross-polar return is zero and the co-polar returns are perfectly correlated. For fully developed speckle the facet scattering cross sections would display an exponential distribution. We assume that the facets are large compared with the small-scale correlation length so that their scattering cross sections are so distributed. This assumption may be too restrictive in future implementations, however it is sufficient to our purposes at this stage.
- 8.6.4 The local incidence angle for the facet is calculated and used with the dielectric and small-scale properties of the surface to calculate the mean backscattering coefficients, according to [36] (Ogilvy, 1991)

$$\mathbf{s}_{ab}^o = 4k^4 \mathbf{s}_s^2 \mathbf{l}_s^2 \cos^4 \mathbf{q}_i \exp(-k^2 \mathbf{l}_s^2 \sin^2 \mathbf{q}_i) |B_{ab}|^2 \quad (8.6.1)$$

8.6.5 The first-order, small perturbation model scattering coefficients in (1) are

$$B_{hh} = \frac{\cos \mathbf{q}_i - \sqrt{\mathbf{e}_s - \sin^2 \mathbf{q}_i}}{\cos \mathbf{q}_i + \sqrt{\mathbf{e}_s - \sin^2 \mathbf{q}_i}} \quad (8.6.2a)$$

$$B_{vv} = \frac{(\mathbf{e}_s - 1)(\sin^2 \mathbf{q}_i - \mathbf{e}_s(1 + \sin^2 \mathbf{q}_i))}{(\mathbf{e}_s \cos \mathbf{q}_i + \sqrt{\mathbf{e}_s - \sin^2 \mathbf{q}_i})^2} \quad (8.6.2b)$$

$$B_{hv} = 0 \quad (8.6.2c)$$

8.6.6 where \mathbf{e}_s is the soil permittivity, calculated according to [47] (Dobson *et al.*, 1985) for a fixed soil type, and \mathbf{q}_i is the *local* incidence angle for the facet.

8.6.7 For each facet we then generate a random number, f , from an exponential distribution, and a random angle, \mathbf{f} , from a uniform distribution on $[0, 2\mathbf{p}]$. The facet scattering amplitude in the *local* frame of the facet is then determined as:

$$\underline{\mathbf{S}}_l = \begin{pmatrix} S_{hhl} & S_{hvl} \\ S_{vhl} & S_{vvl} \end{pmatrix} = \begin{pmatrix} \sqrt{fA\mathbf{s}_{hh}^o} \exp(i\mathbf{f}) & 0 \\ 0 & \sqrt{fA\mathbf{s}_{vv}^o} \exp(i\mathbf{f}) \end{pmatrix} \quad (8.6.3)$$

8.6.8 where A is the facet area. Now to obtain the scattering matrix in the global frame, we might simply rotate this matrix about the radar line-of-sight (LOS) using the facet orientation. To show how this may be achieved suppose the facet has surface normal vector $\mathbf{n} = (n_x, n_y, n_z)$, where, in terms of slopes, s_x and s_y :

$$\mathbf{g}_n = \sqrt{1 + s_x^2 + s_y^2} \quad n_z = 1/\mathbf{g}_n \quad n_x = -s_x/\mathbf{g}_n \quad n_y = -s_y/\mathbf{g}_n \quad (8.6.4)$$

8.6.9 Now in the global frame the scattering amplitude may be achieved through rotation about the LOS through an angle \mathbf{b}_n such that

$$\begin{aligned} \underline{\mathbf{S}} &= \begin{pmatrix} \cos \mathbf{b}_n & -\sin \mathbf{b}_n \\ \sin \mathbf{b}_n & \cos \mathbf{b}_n \end{pmatrix} \begin{pmatrix} S_{hhl} & 0 \\ 0 & S_{vvl} \end{pmatrix} \begin{pmatrix} \cos \mathbf{b}_n & \sin \mathbf{b}_n \\ -\sin \mathbf{b}_n & \cos \mathbf{b}_n \end{pmatrix} \\ &= \begin{pmatrix} \cos \mathbf{b}_n & -\sin \mathbf{b}_n \\ \sin \mathbf{b}_n & \cos \mathbf{b}_n \end{pmatrix} \begin{pmatrix} S_{hhl} \cos \mathbf{b}_n & S_{hhl} \sin \mathbf{b}_n \\ -S_{vvl} \sin \mathbf{b}_n & S_{vvl} \cos \mathbf{b}_n \end{pmatrix} \\ &= \begin{pmatrix} S_{hhl} \cos^2 \mathbf{b}_n + S_{vvl} \sin^2 \mathbf{b}_n & (S_{hhl} - S_{vvl}) \cos \mathbf{b}_n \sin \mathbf{b}_n \\ (S_{hhl} - S_{vvl}) \cos \mathbf{b}_n \sin \mathbf{b}_n & S_{hhl} \sin^2 \mathbf{b}_n + S_{vvl} \cos^2 \mathbf{b}_n \end{pmatrix} \\ &= \begin{pmatrix} S_{hh} & S_{hv} \\ S_{vh} & S_{vv} \end{pmatrix} \end{aligned} \quad (8.6.5)$$

8.6.10 Expressing the scattering matrix in terms of dyadic products of polarisation vectors we have: $\underline{\mathbf{S}} = S_{hhl} \hat{\mathbf{h}}_l \hat{\mathbf{h}}_l + S_{vvl} \hat{\mathbf{v}}_l \hat{\mathbf{v}}_l$ so that

$$S_{hh} = S_{hhl} (\hat{\mathbf{h}} \cdot \hat{\mathbf{h}}_l) (\hat{\mathbf{h}}_l \cdot \hat{\mathbf{h}}) + S_{vvl} (\hat{\mathbf{h}} \cdot \hat{\mathbf{v}}_l) (\hat{\mathbf{v}}_l \cdot \hat{\mathbf{h}}) = S_{hhl} \cos^2 \mathbf{b}_n + S_{vvl} \sin^2 \mathbf{b}_n \quad (8.6.6a)$$

$$S_{hv} = S_{hhl} (\hat{\mathbf{h}} \cdot \hat{\mathbf{h}}_l) (\hat{\mathbf{h}}_l \cdot \hat{\mathbf{v}}) + S_{vvl} (\hat{\mathbf{h}} \cdot \hat{\mathbf{v}}_l) (\hat{\mathbf{v}}_l \cdot \hat{\mathbf{v}}) = (S_{hhl} - S_{vvl}) \cos \mathbf{b}_n \sin \mathbf{b}_n \quad (8.6.6b)$$

$$S_{vh} = S_{hhl} (\hat{\mathbf{v}} \cdot \hat{\mathbf{h}}_l) (\hat{\mathbf{h}}_l \cdot \hat{\mathbf{h}}) + S_{vvl} (\hat{\mathbf{v}} \cdot \hat{\mathbf{v}}_l) (\hat{\mathbf{v}}_l \cdot \hat{\mathbf{h}}) = (S_{hhl} - S_{vvl}) \cos \mathbf{b}_n \sin \mathbf{b}_n \quad (8.6.6c)$$

$$S_{vv} = S_{hhl} (\hat{\mathbf{v}} \cdot \hat{\mathbf{h}}_l) (\hat{\mathbf{h}}_l \cdot \hat{\mathbf{v}}) + S_{vvl} (\hat{\mathbf{v}} \cdot \hat{\mathbf{v}}_l) (\hat{\mathbf{v}}_l \cdot \hat{\mathbf{v}}) = S_{hhl} \sin^2 \mathbf{b}_n + S_{vvl} \cos^2 \mathbf{b}_n \quad (8.6.6d)$$

8.6.11 In terms of our rotation model:

$$\begin{aligned} (\hat{\mathbf{h}} \cdot \hat{\mathbf{h}}_l) &= +\cos \mathbf{b}_n \\ (\hat{\mathbf{h}} \cdot \hat{\mathbf{v}}_l) &= -\sin \mathbf{b}_n \\ (\hat{\mathbf{v}} \cdot \hat{\mathbf{h}}_l) &= +\sin \mathbf{b}_n \\ (\hat{\mathbf{v}} \cdot \hat{\mathbf{v}}_l) &= +\cos \mathbf{b}_n \end{aligned} \quad (8.6.7)$$

8.6.12 By definition we have

$$\hat{\mathbf{h}}_l = \frac{\hat{\mathbf{n}} \times \hat{\mathbf{k}}}{|\hat{\mathbf{n}} \times \hat{\mathbf{k}}|} \quad \hat{\mathbf{v}}_l = \hat{\mathbf{h}}_l \times \hat{\mathbf{k}} \quad (8.6.8)$$

8.6.13 In the simulation (and in fact without loss of generality) we write for the incident wave vector, $\hat{\mathbf{k}} = (0, \sin \mathbf{q}, -\cos \mathbf{q})$, where \mathbf{q} is the *global* incidence angle. Substituting our expressions for the facet surface normal vector and the normalised incident wave vector we find (with $\mathbf{n} = (n_x, n_y, n_z)$):

$$\hat{\mathbf{h}} = \frac{\hat{\mathbf{z}} \times \hat{\mathbf{k}}}{|\hat{\mathbf{z}} \times \hat{\mathbf{k}}|} = -\hat{\mathbf{x}} \frac{\sin \mathbf{q}}{|\sin \mathbf{q}|} = -\hat{\mathbf{x}} = (-1, 0, 0) \quad (8.6.9a)$$

$$\hat{\mathbf{v}} = \hat{\mathbf{h}} \times \hat{\mathbf{k}} = -\hat{\mathbf{y}} \cos \mathbf{q} - \hat{\mathbf{z}} \sin \mathbf{q} = (0, -\cos \mathbf{q}, -\sin \mathbf{q}) \quad (8.6.9b)$$

$$\hat{\mathbf{h}}_l = \frac{\hat{\mathbf{n}} \times \hat{\mathbf{k}}}{|\hat{\mathbf{n}} \times \hat{\mathbf{k}}|} = \frac{[-\hat{\mathbf{x}}(n_y \cos \mathbf{q} + n_z \sin \mathbf{q}) + \hat{\mathbf{y}} n_x \cos \mathbf{q} + \hat{\mathbf{z}} n_x \sin \mathbf{q}]}{[n_x^2 + (n_y \cos \mathbf{q} + n_z \sin \mathbf{q})^2]^{1/2}} \quad (8.6.9c)$$

$$\begin{aligned} \hat{\mathbf{v}}_l &= \hat{\mathbf{h}}_l \times \hat{\mathbf{k}} \\ &= \frac{[-\hat{\mathbf{x}} n_x - \hat{\mathbf{y}}(n_y \cos^2 \mathbf{q} + n_z \cos \mathbf{q} \sin \mathbf{q}) - \hat{\mathbf{z}}(n_z \sin^2 \mathbf{q} + n_y \cos \mathbf{q} \sin \mathbf{q})]}{[n_x^2 + (n_y \cos \mathbf{q} + n_z \sin \mathbf{q})^2]^{1/2}} \end{aligned} \quad (8.6.9d)$$

8.6.14 where $\hat{\mathbf{v}}_l \cdot \hat{\mathbf{h}}_l = 0$. In addition

$$\hat{\mathbf{h}} = (-1, 0, 0) \quad (8.6.10a)$$

$$\hat{\mathbf{v}} = (0, -\cos \mathbf{q}, -\sin \mathbf{q}) \quad (8.6.10b)$$

$$\mathbf{g}_n = [n_x^2 + (n_y \cos \mathbf{q} + n_z \sin \mathbf{q})^2]^{1/2} \quad (8.6.10c)$$

$$\hat{\mathbf{h}}_l = (-n_y \cos \mathbf{q} - n_z \sin \mathbf{q}, n_x \cos \mathbf{q}, n_x \sin \mathbf{q}) / \mathbf{g}_n \quad (8.6.10d)$$

$$\hat{\mathbf{v}}_l = (-n_x, -n_y \cos^2 \mathbf{q} - n_z \cos \mathbf{q} \sin \mathbf{q}, -n_z \sin^2 \mathbf{q} - n_y \cos \mathbf{q} \sin \mathbf{q}) / \mathbf{g}_n \quad (8.6.10e)$$

8.6.15 Therefore

$$\cos \mathbf{b}_n = \hat{\mathbf{h}} \cdot \hat{\mathbf{h}}_l = (n_y \cos \mathbf{q} + n_z \sin \mathbf{q}) / \mathbf{g}_n \quad (8.6.11a)$$

$$\sin \mathbf{b}_n = -(\hat{\mathbf{h}} \cdot \hat{\mathbf{v}}_l) = -n_x / \mathbf{g}_n \quad (8.6.11b)$$

$$\cos \mathbf{b}_n = (\hat{\mathbf{v}} \cdot \hat{\mathbf{v}}_l) = (n_y \cos \mathbf{q} + n_z \sin \mathbf{q}) / \mathbf{g}_n \quad (8.6.11c)$$

$$\sin \mathbf{b}_n = (\hat{\mathbf{v}} \cdot \hat{\mathbf{h}}_l) = -n_x / \mathbf{g}_n \quad (8.6.11d)$$

8.6.16 Thus

$$\tan \mathbf{b}_n = \frac{-n_x}{(n_y \cos \mathbf{q} + n_z \sin \mathbf{q})} = \frac{s_x}{(\sin \mathbf{q} - s_y \cos \mathbf{q})} \quad (8.6.12)$$

8.6.17 [39] (Lee *et al.*, 2000).

8.6.18 So to recap: we may find the angle \mathbf{b}_n from the facet surface normal vector using (12) and form the global scattering matrix from the local scattering matrix using (5) or (6).

8.6.19 Now this is perfectly legitimate and for surfaces which are rough on the large-scale works quite well. However, it is more often the case that surfaces are not very rough on the large-scale, and under these circumstances the polarimetric entropy recovered from the surface term is unrealistically low. To counter this effect we can introduce an additional rotation angle, \mathbf{b} , uniformly distributed between $[-\mathbf{b}_1, +\mathbf{b}_1]$, *à-la*-XBragg [37] (Hajnsek *et al.*, 2003). This helps to increase polarimetric entropy and enhance realism. Thus our final model is in fact XBragg at the small-scale, described by surface roughness, correlation length, soil moisture, and additional tilt angle range.

8.6.20 The value of the range of acceptable XBragg rotation angles may be determined by considering the HHVV coherence, which may now be tailored to a desired value by varying \mathbf{b}_1 . For a surface with zero slopes, and no large-scale roughness, the XBragg model predicts a coherency matrix:

$$\mathbf{k}_P = \frac{1}{\sqrt{2}} [S_{hh} + S_{vv}, S_{hh} - S_{vv}, 2S_{hv}]^T \quad (8.6.13)$$

$$S_{hh} = S_{hhl} (\hat{\mathbf{h}} \cdot \hat{\mathbf{h}}_l) (\hat{\mathbf{h}}_l \cdot \hat{\mathbf{h}}) + S_{vvl} (\hat{\mathbf{h}} \cdot \hat{\mathbf{v}}_l) (\hat{\mathbf{v}}_l \cdot \hat{\mathbf{h}}) = S_{hhl} \cos^2 \mathbf{b} + S_{vvl} \sin^2 \mathbf{b} \quad (8.6.14a)$$

$$S_{hv} = S_{hhl} (\hat{\mathbf{h}} \cdot \hat{\mathbf{h}}_l) (\hat{\mathbf{h}}_l \cdot \hat{\mathbf{v}}) + S_{vvl} (\hat{\mathbf{h}} \cdot \hat{\mathbf{v}}_l) (\hat{\mathbf{v}}_l \cdot \hat{\mathbf{v}}) = (S_{hhl} - S_{vvl}) \cos \mathbf{b} \sin \mathbf{b} \quad (8.6.14b)$$

$$S_{vh} = S_{hhl} (\hat{\mathbf{v}} \cdot \hat{\mathbf{h}}_l) (\hat{\mathbf{h}}_l \cdot \hat{\mathbf{h}}) + S_{vvl} (\hat{\mathbf{v}} \cdot \hat{\mathbf{v}}_l) (\hat{\mathbf{v}}_l \cdot \hat{\mathbf{h}}) = (S_{hhl} - S_{vvl}) \cos \mathbf{b} \sin \mathbf{b} \quad (8.6.14c)$$

$$S_{vv} = S_{hhl} (\hat{\mathbf{v}} \cdot \hat{\mathbf{h}}_l) (\hat{\mathbf{h}}_l \cdot \hat{\mathbf{v}}) + S_{vvl} (\hat{\mathbf{v}} \cdot \hat{\mathbf{v}}_l) (\hat{\mathbf{v}}_l \cdot \hat{\mathbf{v}}) = S_{hhl} \sin^2 \mathbf{b} + S_{vvl} \cos^2 \mathbf{b} \quad (8.6.14d)$$

$$\begin{aligned} \mathbf{k}_P &= \frac{1}{\sqrt{2}} [S_{hhl} + S_{vvl}, (S_{hhl} - S_{vvl})(\cos^2 \mathbf{b} - \sin^2 \mathbf{b}), 2(S_{hhl} - S_{vvl}) \cos \mathbf{b} \sin \mathbf{b}]^T \\ &= \frac{1}{\sqrt{2}} [(S_{hhl} + S_{vvl}), (S_{hhl} - S_{vvl}) \cos 2\mathbf{b}, (S_{hhl} - S_{vvl}) \sin 2\mathbf{b}]^T \end{aligned} \quad (8.6.15)$$

$$2T_{11} = \langle |S_{hh} + S_{vv}|^2 \rangle \quad (8.6.16a)$$

$$2T_{12} = \langle (S_{hh} + S_{vv})(S_{hh} - S_{vv})^* \rangle \langle \cos 2\mathbf{b} \rangle \quad (8.6.16b)$$

$$2T_{22} = \langle |S_{hh} - S_{vv}|^2 \rangle \langle \cos^2 2\mathbf{b} \rangle \quad (8.6.16c)$$

$$2T_{33} = \langle |S_{hh} - S_{vv}|^2 \rangle \langle \sin^2 2\mathbf{b} \rangle \quad (8.6.16d)$$

8.6.21 Where in the XBragg model:

$$\langle \cos 2\mathbf{b} \rangle = \text{Sinc}(2\mathbf{b}_1) \quad (8.6.17a)$$

$$\langle \cos^2 2\mathbf{b} \rangle = \frac{1}{2} [1 + \text{Sinc}(4\mathbf{b}_1)] \quad (8.6.17b)$$

$$\langle \sin^2 2\mathbf{b} \rangle = \frac{1}{2} [1 - \text{Sinc}(4\mathbf{b}_1)] \quad (8.6.17c)$$

8.6.22 Whereas for a surface with non-zero slopes, but zero XBragg rotation range we might have

$$2T_{11} = \langle |S_{hh} + S_{vv}|^2 \rangle \quad (8.6.18a)$$

$$2T_{12} = \langle (S_{hh} + S_{vv})(S_{hh} - S_{vv})^* \rangle \cos 2\mathbf{b}_o \quad (8.6.18b)$$

$$2T_{22} = \langle |S_{hh} - S_{vv}|^2 \rangle \cos^2 2\mathbf{b}_o \quad (8.6.18c)$$

$$2T_{33} = \langle |S_{hh} - S_{vv}|^2 \rangle \sin^2 2\mathbf{b}_o \quad (8.6.18d)$$

8.6.23 For a more general case, with rotation angle $\mathbf{b} = \mathbf{b}_{XBragg} + \mathbf{b}_{facet}$ we may examine the mean co-polar powers and co-polar coherency:

$$\begin{aligned} \langle |S_{hh}|^2 \rangle &= \langle |S_{hh}|^2 \rangle \langle \cos^4 \mathbf{b} \rangle + \langle |S_{vv}|^2 \rangle \langle \sin^4 \mathbf{b} \rangle \\ &+ 2 \text{Re} \{ \langle S_{hh} S_{vv}^* \rangle \} \langle \cos^2 \mathbf{b} \sin^2 \mathbf{b} \rangle \end{aligned} \quad (8.6.19a)$$

$$\begin{aligned} \langle |S_{vv}|^2 \rangle &= \langle |S_{vv}|^2 \rangle \langle \cos^4 \mathbf{b} \rangle + \langle |S_{hh}|^2 \rangle \langle \sin^4 \mathbf{b} \rangle \\ &+ 2 \text{Re} \{ \langle S_{hh} S_{vv}^* \rangle \} \langle \cos^2 \mathbf{b} \sin^2 \mathbf{b} \rangle \end{aligned} \quad (8.6.19b)$$

$$\begin{aligned} \langle S_{hh} S_{vv}^* \rangle &= (\langle |S_{hh}|^2 \rangle + \langle |S_{vv}|^2 \rangle) \langle \cos^2 \mathbf{b} \sin^2 \mathbf{b} \rangle \\ &+ \langle S_{hh} S_{vv}^* \rangle \langle \cos^4 \mathbf{b} \rangle + \langle S_{hh} S_{vv}^* \rangle \langle \sin^4 \mathbf{b} \rangle \end{aligned} \quad (8.6.19c)$$

8.6.24 Since in the Bragg model HH and VV are perfectly correlated so $\langle S_{hh} S_{vv}^* \rangle$ is real and these simplify to:

$$\begin{aligned} \langle |S_{hh}|^2 \rangle &= \langle |S_{hh}|^2 \rangle \langle \cos^4 \mathbf{b} \rangle + \langle |S_{vv}|^2 \rangle \langle \sin^4 \mathbf{b} \rangle \\ &+ 2 \langle S_{hh} S_{vv}^* \rangle \langle \cos^2 \mathbf{b} \sin^2 \mathbf{b} \rangle \end{aligned} \quad (8.6.20a)$$

$$\begin{aligned} \langle |S_{vv}|^2 \rangle &= \langle |S_{vv}|^2 \rangle \langle \cos^4 \mathbf{b} \rangle + \langle |S_{hh}|^2 \rangle \langle \sin^4 \mathbf{b} \rangle \\ &+ 2 \langle S_{hh} S_{vv}^* \rangle \langle \cos^2 \mathbf{b} \sin^2 \mathbf{b} \rangle \end{aligned} \quad (8.6.20b)$$

$$\begin{aligned} \langle S_{hh} S_{vv}^* \rangle &= (\langle |S_{hh}|^2 \rangle + \langle |S_{vv}|^2 \rangle) \langle \cos^2 \mathbf{b} \sin^2 \mathbf{b} \rangle \\ &+ \langle S_{hh} S_{vv}^* \rangle (\langle \cos^4 \mathbf{b} \rangle + \langle \sin^4 \mathbf{b} \rangle) \end{aligned} \quad (8.6.20c)$$

$$\langle |S_{hv}|^2 \rangle = \langle |S_{hhl} - S_{vv}|^2 \rangle = \langle \cos^2 \mathbf{b} \sin^2 \mathbf{b} \rangle \quad (8.6.20d)$$

8.6.25 Note that a value of $\mathbf{b}_1 = \mathbf{p} / 3$ results in a reduced HHVV coherence of ~ 0.94 . Note also that

$$\langle \cos^2 \mathbf{b} \rangle = \frac{1}{2} [1 + \text{Sinc}(2\mathbf{b}_1)] \quad (8.6.21a)$$

$$\langle \sin^2 \mathbf{b} \rangle = \frac{1}{2} [1 - \text{Sinc}(2\mathbf{b}_1)] \quad (8.6.21b)$$

$$\langle \cos^2 \mathbf{b} \sin^2 \mathbf{b} \rangle = \frac{1}{4} \left[\frac{1}{2} (1 + \text{Sinc}(2\mathbf{b}_1)) - \cos^3(\mathbf{b}_1) \text{Sinc}(\mathbf{b}_1) \right] \quad (8.6.21c)$$

8.6.26 and

$$\langle \cos^4 \mathbf{b} \rangle = \langle \cos^2 \mathbf{b} \rangle - \langle \cos^2 \mathbf{b} \sin^2 \mathbf{b} \rangle \quad (8.6.21d)$$

$$\langle \sin^4 \mathbf{b} \rangle = \langle \sin^2 \mathbf{b} \rangle - \langle \cos^2 \mathbf{b} \sin^2 \mathbf{b} \rangle \quad (8.6.21e)$$

8.7 XBragg on a Tilted Surface

8.7.1 Our results so far have been quoted for a uniform, symmetric distribution of XBragg rotation angle. However if the large-scale roughness is zero (i.e. the surface is flat, but rough on the small-scale), but the mean surface has non-zero slopes, then the distribution of rotation angles is offset by an amount determined by the mean slope. Let the mean rotation angle satisfy

$$\tan \mathbf{b}_o = \frac{s_x}{(\sin \mathbf{q} - s_y \cos \mathbf{q})} \quad (8.6.22)$$

8.7.2 where the slopes are those of the mean surface. Our equations for the mean backscattering coefficients and correlation, (20a)-(20d), still hold but the angular brackets denote averaging over the offset distribution. For example we now seek:

$$\begin{aligned} \langle \cos^2(\mathbf{b} + \mathbf{b}_o) \rangle &= \langle (\cos \mathbf{b} \cos \mathbf{b}_o - \sin \mathbf{b} \sin \mathbf{b}_o)^2 \rangle \\ &= \langle \cos^2 \mathbf{b} \rangle \cos^2 \mathbf{b}_o - \langle \sin^2 \mathbf{b} \rangle \sin^2 \mathbf{b}_o \\ &= \frac{\cos^2 \mathbf{b}_o}{2} [1 + \text{Sinc}(2\mathbf{b}_1)] - \frac{\sin^2 \mathbf{b}_o}{2} [1 - \text{Sinc}(2\mathbf{b}_1)] \end{aligned} \quad (8.6.23)$$

$$\begin{aligned} \langle \sin^2(\mathbf{b} + \mathbf{b}_o) \rangle &= \langle (\sin \mathbf{b} \cos \mathbf{b}_o + \cos \mathbf{b} \sin \mathbf{b}_o)^2 \rangle \\ &= \langle \sin^2 \mathbf{b} \rangle \cos^2 \mathbf{b}_o + \langle \cos^2 \mathbf{b} \rangle \sin^2 \mathbf{b}_o \\ &= \frac{\cos^2 \mathbf{b}_o}{2} [1 - \text{Sinc}(2\mathbf{b}_1)] + \frac{\sin^2 \mathbf{b}_o}{2} [1 + \text{Sinc}(2\mathbf{b}_1)] \end{aligned} \quad (8.6.24)$$

$$\begin{aligned} \langle \cos^2(\mathbf{b} + \mathbf{b}_o) \sin^2(\mathbf{b} + \mathbf{b}_o) \rangle &= \langle \cos^2 \mathbf{b} \sin^2 \mathbf{b} \rangle (\cos^4 \mathbf{b}_o + \sin^4 \mathbf{b}_o - 4 \cos^2 \mathbf{b}_o \sin^2 \mathbf{b}_o) \\ &+ (\langle \cos^4 \mathbf{b} \rangle + \langle \sin^4 \mathbf{b} \rangle) \cos^2 \mathbf{b}_o \sin^2 \mathbf{b}_o \end{aligned} \quad (8.6.25)$$

- 8.7.3 These results may be used to estimate the direct ground backscattering coefficients using equations (20) and (21).

8.8 DG Algorithm Summary

- 8.8.1 The DEM is broken into facets and for each facet a speckle phase is assigned from a uniformly random distribution on $[0, 2\pi]$, and a scattering power scaling is generated from an exponential distribution. The mean local scattering powers for the facet are calculated in the SPM using the facet area and orientation, and the local scattering amplitude matrix for the facet is determined from (3). The facet orientation is used to define a LOS rotation angle from (12), and to this is added a random X-Bragg rotation. The global frame scattering amplitude is determined from (6) using the combined rotation angle. Attenuation effects are then incorporated into the scattering amplitude using the lookup table, before focusing the contribution in the SAR image.

8.9 Direct-Vegetation (DV) and Direct-Forest (DF) SAR Images

- 8.9.1 The strategies employed to calculate both the short vegetation and forest contributions are very similar, differing in the main by the scattering models used for plant elements based on dimensions relative to wavelength. Another subtle difference is in the way the totality of the contributions from different classes of scatterer is estimated ...

8.10 Deterministic Model

- 8.10.1 Volume terms for large scatterers, i.e. stems, primary and secondary branches are calculated in a deterministic fashion. Branches are divided into short segments, and scattering is modelled using an approximate but efficient form for the truncated infinite cylinder approximation [40, 41] (Fung, 1994, Karam *et al.*, 1988).

8.11 Hybrid Stochastic Model

- 8.11.1 The numerous small plant elements in each crown and in the short vegetation layer are treated efficiently by using a hybrid approach. When calculating scattering terms the understorey is divided into areas smaller than a resolution cell, and each is populated with a number of random realisations of occupying scattering elements. Crowns are treated in a similar fashion: distributing realizations throughout the crown evenly.
- 8.11.2 Scattering amplitudes are scaled if the number of plant elements that would actually be found in each area or volume is greater than the number of realizations. Realisations are preserved between calculations for each track on the interferometric baseline: in this fashion computational efficiency is

maintained whilst preserving both backscattering coefficient, and coherence behaviour with baseline.

- 8.11.3 Scattering by small elements is calculated using the Rayleigh-Gans approach [32] (Williams and Quegan, 1996), whilst the scattering due to very small objects, such as Pine needles, at low frequency is, if not significant, ignored. These considerations serve to make the calculation computationally efficient.
- 8.11.4 Vegetation dielectric permittivities are calculated according to [46] (Ulaby *et al.*, 1987), using predetermined plant element water contents.

8.12 Surface-Vegetation (SV) and Surface-Forest (SF) SAR Images

- 8.12.1 The calculation of the “effective scattering centre” [10] (Williams, 2006) is a heavy computational burden if we require account to be taken of local slope. Thus the approximation is adopted that the reflection is from the mean terrain surface, and is modulated by the mean roughness. Thus the “effective scattering centre” is found readily for all scatterers as the projection onto the mean terrain surface of the scattering centre [10].
- 8.12.2 Both the deterministic and hybrid stochastic approaches are adopted for the SV calculation in the manners previously described in the DV section. The ground-surface-volume-ground-surface (SVS) interaction is not considered as it is generally found not to be significant. Note that whilst DV terms display layover, the same is not true for SV terms. If included SVS terms would display layover away from the radar, and appear to have phase centres below the soil surface. In the shadow region of the forest stand the SVS term may thus appear dominant and lead to confusing tree height inversions. To avoid this, and the associated high costs of its computation, the SVS term is omitted.

8.13 Summary of Input Parameters

- 8.13.1 The following parameters are required for SAR image generation: frequency, the SAR sensor center frequency in Gigahertz (between L-band, 1.3GHz, and P-band, 0.433GHz), the number of tracks (2 for **PolSARproSim**) required for the interferometry, the broadside slant ranges to scene center (in metres) for each of the specified tracks, the global incidence angles at scene center (in degrees) for each of the specified tracks, the desired final SAR cross range resolution (in metres) specified as the width at half height power of the system point spread function in azimuth, and the desired final SAR slant range resolution (in metres) specified as the width at half height power of the system point spread function in slant range.
- 8.13.2 Note that slant range is assumed constant for each simulated track, as is the system center frequency. Note also that the ground range resolution thus varies from track to track, as calculated in the simulation.
- 8.13.3 In addition there are a number of bio-physical parameters required in order to determine the scattering properties of the scene, such as branch and leaf moisture contents and soil moisture. Of these only soil moisture and surface roughness models are requested from the user on sliding scales from 0 to 10.

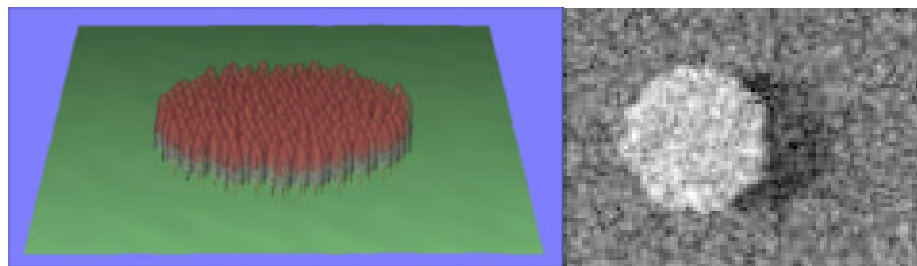


Figure 8.2 Example output from **PolSARproSim**. In this example a forest stand of 16.5m tall pine trees with area 0.39Ha was requested. The view of the forest stand from the radar is on the left. Living crowns are displayed in red, and lower, dry crowns in grey. The stand was imaged at L-band and 70 degrees incidence at a resolution of 3m in azimuth and ground range, yielding images of dimensions 95 pixels in range and 65 in azimuth. The log total power SAR image is on the right. The pine trees display layover towards the radar (left of SAR image) and shadow the short vegetation away from the radar.

9 File Formats and Calling Convention

9.1 Introduction

- 9.1.1 There are a number of files required for the correct operation of the program and their formats are described in this document.

9.2 Input Text File

- 9.2.1 The input parameter file is an ASCII text file with the three-letter extension “**sar**”, e.g. “**run001.sar**”. The following parameters are input to **PolSARproSim** from PolSARpro:

2	/* The number of requested tracks	*/
3192.533	/* Slant range in metres	*/
20.0	/* Incidence angle in degrees	*/
3194.2467	/* Slant range in metres	*/
20.084280	/* Incidence angle in degrees	*/
1.3	/* Centre frequency in GHz	*/
3.0	/* Azimuth resolution in metres	*/
1.026060	/* Slant range resolution in metres	*/
6	/* Ground model: 0 = smoothest ... 10 = roughest	*/
0.001	/* Ground slope in azimuth direction (dimensionless)	*/
0.002	/* Ground slope in ground range direction (dimensionless)	*/
222	/* Random number generator seed	*/
1	/* Tree species: 0 = HEDGE, 1,2,3 = PINE, 4 = DECIDUOUS	*/
16.5	/* Mean tree height in metres	*/
3927.0	/* Area of the forest stand in square metres	*/
550	/* Desired stand density in stems per hectare	*/
4	/* Ground moisture content model: 0 = dry ... 10 = wet	*/

Figure 9.1 An example of the ASCII input file format

- 9.2.2 Each line of the input file consists of an initial value (one per line) followed by optional text describing the parameter associated with the value.
- 9.2.3 Each line of text is terminated by a line feed (LF, ASCII 10, 0x0A) character, or a carriage return character (CR, ASCII 13, 0x0D) or both.
- 9.2.4 The text input file contains sixteen (16) lines, one for each parameter described in the following:
- 9.2.5 The number of requested tracks. This is an int and always has the value two (2) for calls to **PolSARproSim** from within **PolSARPro v2.0**.
- 9.2.6 The next four lines describe the tracks to be simulated for the interferometric pair of SAR images. Each track is parameterised using a slant range (in metres) followed by an incidence angle (in degrees). Slant range values and incidence angle values are input as type double.

- 9.2.7 The centre frequency follows as type double and is given in Gigahertz.
- 9.2.8 The azimuth resolution follows as type double and is given in metres. NOTE the definition of resolution for the purposes of **PoISARproSim** is width of the point spread function at half height in power.
- 9.2.9 The slant-range resolution follows as type double and is given in metres. As with azimuth resolution this is defined as the width of the point spread function at half height in power. The slant-range resolution is held fixed for each track, which corresponds to constant system bandwidth.
- 9.2.10 There then follows an int parameter used to define the ground surface properties. This parameter has the minimum value zero (0), corresponding to the smoothest surface, and the maximum value ten (10), for the roughest surface. This value is translated into actual values of surface height standard deviation and correlation length within **PoISARproSim**.
- 9.2.11 Ground slope in azimuth (type double) is recorded on the next line of the input file: this is a dimensionless quantity describing the slope of the mean underlying surface in the azimuth direction.
- 9.2.12 Ground slope in range (type double) is recorded on the next line of the input file: again this is a dimensionless quantity describing the slope of the mean underlying surface in the azimuth direction.
- 9.2.13 The next line is a type int value used to seed the random number generator.
- 9.2.14 The next line is an int value used to define the species of tree occupying the forest. Possible values are listed in Figure 7.1. Not all of these are operational as only two operational values are officially implemented in this version of **PoISARproSim**. These will include the value zero (0), representing the HEDGE, and one of the values between one (1) and (4). The final choice will depend upon time constraints of the implementation stage, and performance of the final model.
- 9.2.15 The next three lines are used to describe the forest stand. The first is a double representing the mean height of trees in metres.
- 9.2.16 The next double is the area of the forest stand in square metres.
- 9.2.17 The next int is the forest stand density given as the number of trees per hectare.
- 9.2.18 Finally an int value is used to describe the requested soil moisture level.
- 9.2.19 Note that the SAR image area and final image dimensions are determined using these parameters and other "hard-wired" values such as sampling rate etc.
- 9.2.20 Note also that these values are "requested" values. The actual values used within the simulation may not correspond exactly to these values. However the

internal parameter values will be close to those requested, and the actual values used are output into a text file with the extension ".out".

- 9.2.21 The output text file is stored in the requested master directory. This brings us to the format for calling the simulation from within **PolSARPro**.

9.3 *PolSARproSim Calling Convention*

- 9.3.1 **PolSARproSim** is called with three arguments:

```
config_file_prefix master_directory slave_directory
```

- 9.3.2 That is to say the executable is called with name **PolSARproSim** or **PolSARproSim.exe** and is passed three string variables on the command line. The first variable is the input/output filename prefix, including the directory path, the second is the pathname of the directory where **PolSARproSim** is to write output for the base track, and the third is the directory where **PolSARproSim** will write output for the second track. For example the arguments

```
C:\Workspace\test C:\Workspace\Master C:\Workspace\Slave
```

- 9.3.3 will cause the simulation to read input from the file with name “**test.sar**” in the directory “**C:\Workspace**”, and to write output to the directories “**C:\Workspace\Master**” and “**C:\Workspace\Slave**”.
- 9.3.4 Aside from the polarimetric SAR imagery, which is output in binary form (formats are discussed later), other forms of output include a graphic file with a simplified representation of the simulated forest stand as viewed from the platform at broadside, a large-scale ground height map, and attenuation mapping data. In addition the simulation writes three text files in the master directory: **prefix_call.txt**, **prefix.out** and **prefix.log**. The first of these simply details the call made to **PolSARproSim**, the second reproduces the contents of the input file, and lists the details of the SAR images produced. The log file contains detailed information about the performance of **PolSARproSim** and is maintained for debugging and trouble-shooting purposes, and is not intended for the user.

9.4 Graphic File Format

- 9.4.1 Following the input of parameters and construction of the forest scene a small graphic image is calculated and output as a guide to the visual interpretation of the resulting SAR images.
- 9.4.2 Graphic image files have the extension “**gri**”. A single image is output to the master directory with the name “**forest_image.gri**”.
- 9.4.3 Procedures for reading and writing the graphic image files are provided as part of **PolSARproSim** and may be called from within **PolSARPro**. This library is self-contained and defined in the files “**GraphicImage.h**” and “**GraphicImage.c**”.
- 9.4.4 Graphics files with the extension “**.gri**” are binary files with the following format:

long	:	np, the total number of pixels in the image
int	:	nx, the number of pixels in the “x”-direction
int	:	ny, the number of pixels in the “y”-direction
int	:	n, the number of char bytes in the filename
n×char	:	the filename
int	:	Ninfo, the number of bytes of ancillary text information
Ninfo×char	:	the ancillary text information
n×graphic_pixel	:	the image data

Figure 9.2 The graphic image file format

- 9.4.5 The type **graphic_pixel** is defined as follows:

```
typedef struct graphic_pixel_tab {
    unsigned char red;
    unsigned char green;
    unsigned char blue;
} graphic_pixel;
```

Figure 9.3 The **graphic_pixel** record definition

- 9.4.6 The image data is written as a single block with equivalent statement:


```
fwrite (pGI, sizeof (graphic_pixel), np, pGF);
```
- 9.4.7 where in the above **pGI** is of type **graphic_pixel*** and **pGF** is of type **FILE***.
- 9.4.8 When run in the windows environment **PolSARproSim** will also output a Windows BMP format version of the graphic image called “**forest_image.bmp**”.

9.5 Image File Format

- 9.5.1 SAR imagery is output in binary form as defined in the PolSARpro Manual.
- 9.5.2 In addition **PolSARproSim** has its own file format for handling non-graphic images. This format is used to output the ground height map and attenuation maps.
- 9.5.3 Procedures for reading and writing the **PolSARproSim** image files are provided as part of **PolSARproSim** and may be called from within **PolSARPro**. This library is self-contained and defined in the files “**SarImage.h**” and “**SarImage.c**”.
- 9.5.4 **PolSARproSim** image files have the extension “**.sim**”, and the following format:

double	:	dx, the pixel dimension in the “x”-direction
double	:	dy, the pixel dimension in the “y”-direction
int	:	n, the number of char bytes in the filename
n`char	:	the filename
double	:	Lx, the SAR image dimension in the “x”-direction
double	:	Ly, the SAR image dimension in the “y”-direction
int	:	Ninfo, the number of bytes of ancillary text information
long	:	np, the total number of pixels in the image
int	:	nx, the number of pixels in the “x”-direction
int	:	ny, the number of pixels in the “y”-direction
Ninfo`char	:	the ancillary text information
int	:	pixel type (see figure 7.4.2)
n`sim_pixel	:	the image data

Figure 9.4 The SAR image file format

- 9.5.5 The type `sim_pixel` is defined as follows:

```
typedef struct sim_float_complex_tag {
    float x;
    float y;
} SIM_Complex_Float;

typedef struct sim_double_complex_tag {
    double x;
    double y;
} SIM_Complex_Double;

typedef unsigned char      sim_byte;
typedef unsigned short int sim_word;
typedef int                sim_dword;
typedef float              sim_float;
typedef double             sim_double;
typedef SIM_Complex_Float  sim_complex_float;
typedef SIM_Complex_Double sim_complex_double;

typedef union sim_type_tag {
    sim_byte      b;
    sim_word      w;
    sim_dword     dw;
}
```

```

sim_float          f;
sim_double         d;
sim_complex_float  cf;
sim_complex_double cd;
} sim_type;

typedef struct simpixel_tag {
    int          simpixeltype;
    sim_type     data;
} sim_pixel;

```

Figure 9.5 The SAR image sar_pixel type definition.

9.5.6 **PolSARproSim** outputs the following files in the master directory:

ground_height.sim, AmapDirectV.sim, AmapDirectH.sim, AmapBounceV.sim, and AmapBounceH.sim.

10 References

- [1] Christian Ruiz and Pierre Borderies (ONERA, France), *Sensitivity analysis for forest interferometric, polarimetric observables estimation*, Proc. PolInSAR 2005.
- [2] Jaan Praks *et al.* (HUT, Finland), *Simulation of Polarimetric Scattering from Forest Canopy*, Proceedings of XXVII URSI/IEEE Convention on Radio Science, 2002.
- [3] Prof. J A Kong (MIT, USA), *Electromagnetic Theory and Applications, Research on SAR Simulation Model*, RLE Progress Report 144.
- [4] Paul A Stuopis *et al.* (Nevada, USA) *The modeling of forested areas for real and synthetic aperture imaging radar simulation*, Proceedings, IGARSS '96: 1996
- [5] K Sarabandi and Y-C Lin (Michigan, USA), *Simulation of Interferometric SAR Response to Deciduous and Coniferous Forest Stands*, Proc. IGARSS97, 1997.
- [6] Y-C Lin and K Sarabandi, *A Monte Carlo Coherent Scattering Model for Forest Canopies using Fractal Generated Trees*, IEEE Trans. Geo. Rem. Sens., **37**, #1, p440, 1999.
- [7] C Varenkamp and D H Hoekman (Netherlands), *High-Resolution InSAR Image Simulation for Forest Canopies*, IEEE Trans. Geo. Rem. Sens., **40**, #7, p1648, 2002.
- [8] S R Cloude, D G Corr and M L Williams, *Target Detection Beneath Foliage using Polarimetric Synthetic Aperture Radar Interferometry*, Waves in Random Media, **14**, S393-S414, 2004.
- [9] F Lombardini and M L Williams, *SAR Tomography with Simulated Data*, Proceedings EUSAR 2006.
- [10] M L Williams, *The Theory for a Forward SAR Model: Implementation, Applications and Challenges*, Proceedings EUSAR 2006.
- [11] M L Williams, R M Lucas, A Lee and S R Cloude, *The Potential of New SAR Sensors for PolInSAR over Australian Forests*, Proceedings EUSAR 2006.
- [12] T L Ainsworth, M L Williams, T Payne and J S Lee, *Polarimetric Variability of Simulated Vegetation Groundcover*, Proceedings EUSAR 2006.
- [13] R Lucas, A Lee and M L Williams, *The Role of LiDAR Data and SAR Simulation in Understanding the Relationship Between Forest Structure and SAR Imagery*, IEEE Transactions on Geoscience and Remote Sensing (accepted August 2006).
- [14] M L Williams, *Physics-Based Modelling for Microwave Remote Sensing: Successes and Challenges*, Progress in Radar Research Workshop, Adelaide, November, 2005.
- [15] R M Lucas, A Lee and M L Williams, *Validation of a Forest SAR Simulation using Fine Remote Sensing and Field Data*, CEOS SAR Cal/Val Workshop, Adelaide, September, 2005.
- [16] M L Williams and S R Cloude, *A Coherent Forest Synthetic Aperture Radar Calculation for PolInSAR Studies*, Progress in Electromagnetics Research Symposium, Hangzhou, China, August 2005.
- [17] M L Williams and S R Cloude, *Predictions of SAR Polarimetry and InSAR Coherence for a Model Wheat Canopy*, Proceedings International Geoscience and Remote Sensing Symposium, Seoul, Korea, July 2005.

- [18] R Lucas, A Lee and M L Williams, *The Role of LiDAR Data in Understanding the Relationship Between Forest Structure and SAR Imagery*, Proceedings International Geoscience and Remote Sensing Symposium, Seoul, Korea, July 2005.
- [19] S R Cloude and M L Williams, *The Negative Alpha Filter: A New Processing Technique for Polarimetric SAR Interferometry*, IEEE Geoscience and Remote Sensing Letters, accepted January 2005.
- [20] S R Cloude, D G Corr and M L Williams, *FOPEN using Polarimetric SAR Interferometry*, Proceedings of EUSAR 2004, p. 255, Ulm, Germany, 2004
- [21] M L Williams and G Blucher, *Enhancing FOPEN Performance at L-Band using SAR Polarimetry*, Proceedings of EUSAR 2004, p. 219, Ulm, Germany, 2004
- [22] M L Williams, N Harris and A Beaney, *Reduced False Alarm Rates in Simulated Polarimetric SAR Imagery of Concealed Targets*, Journal of Defence Science, p. R122, 8, #2, May 2003
- [23] M L Williams, T Manninen, S Kellomaki, V-P Ikonen, R Sievanen, M Lehtonen, E Nikinmaa and T Vesala, *Modeling the SAR Response of Pine Forest in Southern Finland*, Proceedings of the International Geoscience and Remote Sensing Symposium, vol. II, pp. 1350-1352, Toulouse 2003
- [24] S R Cloude and M L Williams, *A Coherent EM Scattering Model for Dual Baseline PolInSAR*, Proceedings of the International Geoscience and Remote Sensing Symposium, vol. III, pp. 1423-1425, Toulouse 2003
- [25] M L Williams and N Harris, *Demonstration of Reduced False Alarm Rates using Simulated L-Band Polarimetric SAR Imagery of Concealed Targets*, Proceedings of the International Conference on Radar, p. 535-540, Adelaide, Australia, September 2003
- [26] S R Cloude, D G Corr and M L Williams, *Target Detection beneath Foliage using Polarimetric Synthetic Aperture Radar Interferometry*, Waves in Random Media 14 (2004) p. S393-S414
- [27] M L Williams, *A Study of Low Frequency SAR Clutter using Model Forests*, Proceedings, International Geoscience and Remote Sensing Symposium, Honolulu, Hawaii, 24-28 July 2000
- [28] M L Williams, *Simulation of Low Frequency SAR Clutter from a Pine Forest*, EUSAR 2000, Munich, 24-28 May 2000
- [29] M L Williams, *Prediction and Observation of SAR Clutter from Vegetation Canopies*, Proceedings, International Geoscience and Remote Sensing Symposium, Hamburg, June 1999
- [30] M. L. Williams, *Influence of Canopy Shape on SAR Speckle Distributions over Woodland*, Proceedings of the International Geoscience and Remote Sensing Symposium, Singapore, 3-8 August, IEEE, pp 755-757, 1997.
- [31] M. L. Williams, S. Quegan and D. Blacknell, *Distribution of Backscattered Intensity in the Distorted Born Approximation: Application to C-band SAR images of Woodland*, Waves in Random Media, 7, pp 643-660, 1997.
- [32] M. L. Williams and S. Quegan, *Modelling Microwave Backscatter from Discrete Random Media using Multiple-Scattering Series: Convergence Issues*, Waves in Random Media, 7, pp 213-227, 1996.
- [33] M. L. Williams, *Image Statistics in the Distorted Born Approximation: Application to C-band SAR Images of Dense Woodland*, Progress in Electromagnetics Research Symposium, p 627, Innsbruck, Austria, 8-12 July, 1996.

- [34] M. L. Williams, *Neumann Series: Convergence and Monte Carlo Techniques in the Modelling of Microwave Backscatter*, Progress in Electromagnetics Research Symposium, Seattle, Washington, USA, 24-28 July, 1995.
- [35] S Quegan and M. L. Williams, *Discrete Scatterer and Wave Models for SAR Data: Successes, Links and Limitations*, Report under subcontract Y/282/9601 for Marconi Research Centre under contract 10644/93/NL/NB for the European Space Agency, 1994.
- [36] J A Ogilvy, *Theory of Scattering from Random Rough Surfaces*, IOP, 1991.
- [37] I Hajnsek, E Pottier and S R Cloude, *Inversion of Polarimetric Parameters from Polarimetric SAR*, IEEE Transaction on Geoscience and Remote Sensing, 41, 4, April, 2003.
- [38] L Tsang, J A Kong and R T Shin, *Theory of Microwave Remote Sensing*, Wiley Series in Remote Sensing, 1985.
- [39] Lee, J.-S., Schuler, D. L. and Ainsworth, T. L., IEEE Trans. Geosci. Rem. Sensing, Vol. 38, No. 5, 2000, pp. 2153-2163.
- [40] A K Fung, *Microwave Scattering and Emission Models and their Applications*, Artech House, 1994.
- [41] M A Karam, A K Fung and Y M M Antar, *Electromagnetic Wave Scattering from Some Vegetation Samples*, IEEE Transactions on Geoscience and Remote Sensing, **26**, 6, p799, 1988.
- [42] L Tsang, J A Kong, K-H Ding, C O Ao, *Scattering of Electromagnetic Waves Numerical Simulations*, Wiley Series in Remote Sensing, 2001.
- [43] K. Binder (Ed.), *Monte Carlo Methods in Statistical Physics*, Springer-Verlag, Topics in Current Physics, 1979.
- [44] J Weber and J Penn, *Creation and Rendering of Realistic Trees*, Proceedings, International Conference on Computer Graphics and Interactive Techniques, p119, 1995.
- [45] B Lintermann and O Deussen, *Interactive Modelling of Plants*, IEEE Computer Graphics and Applications, p56, January/February, 1999.
- [46] F T Ulaby and M A El-Rayes, *Microwave Dielectric Spectrum of Vegetation: II. Dual Dispersion Model*, IEEE Transactions on Geoscience and Remote Sensing, **25**, p550, 1987.
- [47] M C Dobson, F T Ulaby, M Hallikainen and M A El-Rayes, *Microwave Dielectric Behaviour of Wet Soil: II. Four-Component Dielectric Mixing Models*, IEEE Transactions on Geoscience and Remote Sensing, **23**, p35, 1985.

11 Appendix A: Finding Ray Intersections

11.1 General

11.1.1 In all cases we define a ray with:

11.1.2 start position \mathbf{p} ,

11.1.3 direction $\hat{\mathbf{a}}$, and

11.1.4 point of intersection $\mathbf{s} = \mathbf{p} + \mathbf{a} \hat{\mathbf{a}}$.

11.2 Intersection with a Plane

11.2.1 Let the plane have normal unit vector $\hat{\mathbf{n}}_p$ and pass through the point \mathbf{p}_0 . Let the unit vectors $\hat{\mathbf{x}}_p$ and $\hat{\mathbf{y}}_p$, lying in the plane, form an orthonormal set with $\hat{\mathbf{n}}_p$. The point of intersection is a solution of:

$$\mathbf{s} = \mathbf{p} + \mathbf{a} \hat{\mathbf{a}} = \mathbf{p}_0 + A \hat{\mathbf{x}}_p + B \hat{\mathbf{y}}_p \quad (11.2.1)$$

11.2.2 From which it follows that if $|\hat{\mathbf{a}} \cdot \hat{\mathbf{n}}_p| > 0$ then

$$\mathbf{a} = (\mathbf{p}_0 - \mathbf{p}) \cdot \hat{\mathbf{n}}_p / (\hat{\mathbf{a}} \cdot \hat{\mathbf{n}}_p) \quad (11.2.2)$$

otherwise there is no intersection. Note that it is possible to find $\mathbf{a} < 0$ and the success of the algorithm will depend upon the sign of alpha when looking for branch lengths.

11.3 Intersection with a Cylinder

11.3.1 Let the cylinder have axial unit vector $\hat{\mathbf{z}}_c$ passing through the base point \mathbf{c}_0 . Let the unit vectors $\hat{\mathbf{x}}_c$ and $\hat{\mathbf{y}}_c$, form an orthonormal set with $\hat{\mathbf{z}}_c$. The point of intersection is a solution of:

$$\begin{aligned} \mathbf{s} &= \mathbf{p} + \mathbf{a} \hat{\mathbf{a}} \\ &= \mathbf{c}_0 + z_s \hat{\mathbf{z}}_c + R(\cos \mathbf{q}_s \hat{\mathbf{x}}_c + \sin \mathbf{q}_s \hat{\mathbf{y}}_c) \end{aligned} \quad (11.3.1)$$

11.3.2 It follows that

$$\hat{\mathbf{z}}_c \cdot \mathbf{s} = (\hat{\mathbf{z}}_c \cdot \mathbf{p}) + \mathbf{a} (\hat{\mathbf{z}}_c \cdot \hat{\mathbf{a}}) = (\hat{\mathbf{z}}_c \cdot \mathbf{c}_0) + z_s \quad (11.3.2a)$$

$$\hat{\mathbf{x}}_c \cdot \mathbf{s} = (\hat{\mathbf{x}}_c \cdot \mathbf{p}) + \mathbf{a} (\hat{\mathbf{x}}_c \cdot \hat{\mathbf{a}}) = (\hat{\mathbf{x}}_c \cdot \mathbf{c}_0) + R \cos \mathbf{q}_s \quad (11.3.2b)$$

$$\hat{\mathbf{y}}_c \cdot \mathbf{s} = (\hat{\mathbf{y}}_c \cdot \mathbf{p}) + \mathbf{a} (\hat{\mathbf{y}}_c \cdot \hat{\mathbf{a}}) = (\hat{\mathbf{y}}_c \cdot \mathbf{c}_0) + R \sin \mathbf{q}_s \quad (11.3.2c)$$

11.3.3 We need only use the last two equations to recover an expression for \mathbf{a} as the solution to a quadratic equation:

$$[(\hat{\mathbf{x}}_c \cdot (\mathbf{p} - \mathbf{c}_0)) + \mathbf{a} (\hat{\mathbf{x}}_c \cdot \hat{\mathbf{a}})]^2 + [(\hat{\mathbf{y}}_c \cdot (\mathbf{p} - \mathbf{c}_0)) + \mathbf{a} (\hat{\mathbf{y}}_c \cdot \hat{\mathbf{a}})]^2 = R^2 \quad (11.3.3)$$

11.3.4 writing

$$A = \hat{\mathbf{x}}_c \cdot (\mathbf{p} - \mathbf{c}_0), \quad B = (\hat{\mathbf{x}}_c \cdot \hat{\mathbf{a}}), \quad C = \hat{\mathbf{y}}_c \cdot (\mathbf{p} - \mathbf{c}_0), \quad D = (\hat{\mathbf{y}}_c \cdot \hat{\mathbf{a}}) \quad (11.3.4)$$

11.3.5 then

$$\mathbf{a}^2 (B^2 + D^2) + 2(AB + CD)\mathbf{a} + (A^2 + C^2 - R^2) = 0 \quad (11.3.5)$$

11.3.6 so that

$$\mathbf{a} = \frac{-(AB + CD) \pm \sqrt{(AB + CD)^2 - (B^2 + D^2)(A^2 + C^2 - R^2)}}{(B^2 + D^2)} \quad (11.3.6)$$

Note that if the argument to the square root is negative the ray does not intersect the cylinder. Also if both B and D are zero then the ray direction is parallel with the cylinder axis and we have either no intersection or an infinity of intersections if the ray lies in the cylinder surface. Otherwise there are two solutions, and the choice of solution will depend upon the application. Let's define a function that performs this operation.

11.4 Intersection with a Cone

11.4.1 Let the cone have axial unit vector $\hat{\mathbf{z}}_c$ passing through the base point \mathbf{c}_0 to the tip of the cone at $\mathbf{t}_c = \mathbf{c}_0 + h \hat{\mathbf{z}}_c$. Let the unit vectors $\hat{\mathbf{x}}_c$ and $\hat{\mathbf{y}}_c$, form an orthonormal set with $\hat{\mathbf{z}}_c$. The point of intersection is a solution of:

$$\begin{aligned} \mathbf{s} &= \mathbf{p} + \mathbf{a} \hat{\mathbf{a}} \\ &= \mathbf{c}_0 + z_s \hat{\mathbf{z}}_c + R(z_s)(\cos \mathbf{q}_s \hat{\mathbf{x}}_c + \sin \mathbf{q}_s \hat{\mathbf{y}}_c), \quad 0 \leq z_s \leq h \end{aligned} \quad (11.4.1)$$

11.4.2 Note that

$$R(z_s) = (h - z_s) \tan(\mathbf{b}) \quad (11.4.2)$$

11.4.2 It follows that

$$\hat{\mathbf{z}}_c \cdot \mathbf{s} = (\hat{\mathbf{z}}_c \cdot \mathbf{p}) + \mathbf{a} (\hat{\mathbf{z}}_c \cdot \hat{\mathbf{a}}) = (\hat{\mathbf{z}}_c \cdot \mathbf{c}_0) + z_s \quad (11.4.3a)$$

$$\hat{\mathbf{x}}_c \cdot \mathbf{s} = (\hat{\mathbf{x}}_c \cdot \mathbf{p}) + \mathbf{a} (\hat{\mathbf{x}}_c \cdot \hat{\mathbf{a}}) = (\hat{\mathbf{x}}_c \cdot \mathbf{c}_0) + R(z_s) \cos \mathbf{q}_s \quad (11.4.3b)$$

$$\hat{\mathbf{y}}_c \cdot \mathbf{s} = (\hat{\mathbf{y}}_c \cdot \mathbf{p}) + \mathbf{a} (\hat{\mathbf{y}}_c \cdot \hat{\mathbf{a}}) = (\hat{\mathbf{y}}_c \cdot \mathbf{c}_0) + R(z_s) \sin \mathbf{q}_s \quad (11.4.3c)$$

11.4.3 We need to recover an expression for \mathbf{a} as the solution to a quadratic equation:

$$[(\hat{\mathbf{x}}_c \cdot (\mathbf{p} - \mathbf{c}_0)) + \mathbf{a} (\hat{\mathbf{x}}_c \cdot \hat{\mathbf{a}})]^2 + [(\hat{\mathbf{y}}_c \cdot (\mathbf{p} - \mathbf{c}_0)) + \mathbf{a} (\hat{\mathbf{y}}_c \cdot \hat{\mathbf{a}})]^2 = R(z_s)^2 \quad (11.4.4)$$

$$R^2(z_s) = (h - z_s)^2 \tan^2(\mathbf{b}) \quad (11.4.5)$$

$$z_s = (\hat{\mathbf{z}}_c \cdot (\mathbf{p} - \mathbf{c}_0)) + \mathbf{a} (\hat{\mathbf{z}}_c \cdot \hat{\mathbf{a}}) \quad (11.4.6)$$

11.4.4 writing

$$A = \hat{\mathbf{x}}_c \cdot (\mathbf{p} - \mathbf{c}_0), \quad B = (\hat{\mathbf{x}}_c \cdot \hat{\mathbf{a}}), \quad C = \hat{\mathbf{y}}_c \cdot (\mathbf{p} - \mathbf{c}_0) \quad (11.4.7)$$

$$D = (\hat{\mathbf{y}}_c \cdot \hat{\mathbf{a}}), \quad E = \hat{\mathbf{z}}_c \cdot (\mathbf{p} - \mathbf{c}_0), \quad F = (\hat{\mathbf{z}}_c \cdot \hat{\mathbf{a}}) \quad (11.4.8)$$

11.4.5 We have

$$[A + \mathbf{a} B]^2 + [C + \mathbf{a} D]^2 = (h - E - \mathbf{a} F)^2 \tan^2(\mathbf{b}) \quad (11.4.9)$$

11.4.6 which is quadratic in \mathbf{a} . Expanding:

$$[A + \mathbf{a} B]^2 + [C + \mathbf{a} D]^2 = (h - E - \mathbf{a} F)^2 \tan^2(\mathbf{b}) \quad (11.4.10)$$

$$\begin{aligned} & \mathbf{a}^2 (B^2 + D^2) + 2(AB + CD)\mathbf{a} + (A^2 + C^2) \\ &= [(h - E) - \mathbf{a} F]^2 \tan^2(\mathbf{b}) \\ &= [(h - E)^2 + \mathbf{a}^2 F^2 - 2F(h - E)\mathbf{a}] \tan^2(\mathbf{b}) \end{aligned} \quad (11.4.11)$$

$$\begin{aligned} & \mathbf{a}^2 (B^2 + D^2 - F^2 \tan^2(\mathbf{b})) + 2(AB + CD + F(h - E) \tan^2(\mathbf{b}))\mathbf{a} \\ &+ (A^2 + C^2 - (h - E)^2 \tan^2(\mathbf{b})) = 0 \end{aligned} \quad (11.4.12)$$

$$a\mathbf{a}^2 + b\mathbf{a} + c = 0 \quad (11.4.13)$$

$$a = B^2 + D^2 - F^2 \tan^2(\mathbf{b}) \quad (11.4.14)$$

$$b = 2(AB + CD + F(h - E) \tan^2(\mathbf{b})) \quad (11.4.15)$$

$$c = A^2 + C^2 - (h - E)^2 \tan^2(\mathbf{b}) \quad (11.4.16)$$

11.4.7 So that \mathbf{a} has solution

$$\mathbf{a} = \frac{-b \pm \sqrt{b^2 - 4ac}}{2a} \quad (11.4.17)$$

The same caveats apply: if the denominator is zero, or if the argument to the square root is negative then there is no solution, otherwise two solutions will exist and these should not lie beyond the tip of the cone.

11.5 Intersection with a Spheroid

11.5.1 Let the spheroid have axial unit vector $\hat{\mathbf{z}}_s$ passing through the base point \mathbf{c}_0 to the tip of the spheroid at $\mathbf{t}_s = \mathbf{c}_0 + h \hat{\mathbf{z}}_s$. Note that the spheroid has semi-axes a_1 (major, $\hat{\mathbf{z}}_s$) direction and a_2 (minor) and that $0 \leq h \leq 2a_1$. Let the unit vectors $\hat{\mathbf{x}}_s$ and $\hat{\mathbf{y}}_s$, form an orthonormal set with $\hat{\mathbf{z}}_s$. The point of intersection is a solution of:

$$\begin{aligned} \mathbf{s} &= \mathbf{p} + \mathbf{a} \hat{\mathbf{a}} \\ &= \mathbf{c}_0 + z_s \hat{\mathbf{z}}_s + R(z_s)(\cos \mathbf{q}_s \hat{\mathbf{x}}_s + \sin \mathbf{q}_s \hat{\mathbf{y}}_s), \quad 0 \leq z_s \leq h \end{aligned} \quad (11.5.1)$$

11.5.2 Note that now we have for the spheroid radius

$$R^2(z_s) = \tan^2(\mathbf{b}) [a_1^2 - (a_1 - h + z_s)^2], \quad \tan \mathbf{b} = a_2 / a_1 \quad (11.5.2)$$

11.5.3 Following our previous analysis:

$$\hat{\mathbf{z}}_s \cdot \mathbf{s} = (\hat{\mathbf{z}}_s \cdot \mathbf{p}) + \mathbf{a} (\hat{\mathbf{z}}_s \cdot \hat{\mathbf{a}}) = (\hat{\mathbf{z}}_s \cdot \mathbf{c}_0) + z_s \quad (11.5.3a)$$

$$\hat{\mathbf{x}}_s \cdot \mathbf{s} = (\hat{\mathbf{x}}_s \cdot \mathbf{p}) + \mathbf{a} (\hat{\mathbf{x}}_s \cdot \hat{\mathbf{a}}) = (\hat{\mathbf{x}}_s \cdot \mathbf{c}_0) + R(z_s) \cos \mathbf{q}_s \quad (11.5.3b)$$

$$\hat{\mathbf{y}}_s \cdot \mathbf{s} = (\hat{\mathbf{y}}_s \cdot \mathbf{p}) + \mathbf{a} (\hat{\mathbf{y}}_s \cdot \hat{\mathbf{a}}) = (\hat{\mathbf{y}}_s \cdot \mathbf{c}_0) + R(z_s) \sin \mathbf{q}_s \quad (11.5.3c)$$

11.5.4 We need to recover an expression for \mathbf{a} as the solution to a quadratic equation:

$$[(\hat{\mathbf{x}}_s \cdot (\mathbf{p} - \mathbf{c}_0)) + \mathbf{a} (\hat{\mathbf{x}}_s \cdot \hat{\mathbf{a}})]^2 + [(\hat{\mathbf{y}}_s \cdot (\mathbf{p} - \mathbf{c}_0)) + \mathbf{a} (\hat{\mathbf{y}}_s \cdot \hat{\mathbf{a}})]^2 = R(z_s)^2 \quad (11.5.4a)$$

$$z_s = (\hat{\mathbf{z}}_s \cdot (\mathbf{p} - \mathbf{c}_0)) + \mathbf{a} (\hat{\mathbf{z}}_s \cdot \hat{\mathbf{a}}) \quad (11.5.4b)$$

11.5.5 writing

$$A = \hat{\mathbf{x}}_s \cdot (\mathbf{p} - \mathbf{c}_0) \quad B = (\hat{\mathbf{x}}_s \cdot \hat{\mathbf{a}}) \quad C = \hat{\mathbf{y}}_s \cdot (\mathbf{p} - \mathbf{c}_0) \quad (11.5.5a)$$

$$D = (\hat{\mathbf{y}}_s \cdot \hat{\mathbf{a}}) \quad E = \hat{\mathbf{z}}_s \cdot (\mathbf{p} - \mathbf{c}_0) \quad F = (\hat{\mathbf{z}}_s \cdot \hat{\mathbf{a}}) \quad (11.5.5b)$$

11.5.6 We have

$$\begin{aligned} & \mathbf{a}^2 (B^2 + D^2 + F^2 \tan^2(\mathbf{b})) \\ & + 2(AB + CD + F(a_1 - h + E) \tan^2(\mathbf{b})) \mathbf{a} \\ & + (A^2 + C^2) - [a_1^2 - (a_1 - h + E)^2] \tan^2(\mathbf{b}) = 0 \end{aligned} \quad (11.5.6)$$

11.5.7 Which we write as

$$a \mathbf{a}^2 + b \mathbf{a} + c = 0 \quad (11.5.7)$$

11.5.8 with

$$a = B^2 + D^2 + F^2 \tan^2(\mathbf{b}) \quad (11.5.8a)$$

$$b = 2(AB + CD + F(a_1 - h + E) \tan^2(\mathbf{b})) \quad (11.5.8b)$$

$$c = (A^2 + C^2) - [a_1^2 - (a_1 - h + E)^2] \tan^2(\mathbf{b}) \quad (11.5.8c)$$

11.5.9 So that \mathbf{a} again has solution

$$\mathbf{a} = \frac{-b \pm \sqrt{b^2 - 4ac}}{2a} \quad (11.5.9)$$

11.5.10 The same caveats apply: if the denominator is zero, or if the argument to the square root is negative then there is no solution, otherwise two solutions will exist and these should not lie beyond the tip of the spheroid.